Renewable and Sustainable Energy Reviews 91 (2018) 287–300

Contents lists available at ScienceDirect

Renewable and Sustainable Energy Reviews

journal homepage: www.elsevier.com/locate/rser

Molybdenum carbide nanoparticle: Understanding the surface properties and reaction mechanism for energy production towards a sustainable future

Peter Adeniyi Alaba[a,*], Ali Abbas[c], Jun Huang[c], Wan Mohd Ashri Wan Daud[b]

[a] Department of Chemical Engineering, Covenant University, Sango-ota, Ogun-State, Nigeria
[b] Department of Chemical Engineering, University of Malaya, 50603 Kuala Lumpur, Malaysia
[c] School of Chemical and Biomolecular Engineering, University of Sydney, NSW 2006, Australia

ARTICLE INFO

Keywords:
Molybdenum carbide nanoparticle
Hydrogenation
Hydrogen evolution reaction
Extreme learning machine
Multiscale

ABSTRACT

Rational design and synthesis of cheap, noble metal-free, thermal/hydrothermal stable and active catalyst for efficient hydrogenation and hydrogen production reaction is crucial towards renewable and sustainable energy generation. This gives the use of molybdenum carbide nanoparticle considerable attention as an alternative to noble metals. However, the industrial application is not yet feasible due to insufficient stability and activity coupled with the lack of detailed understanding of the reaction mechanism. This work discusses the effect of the operating parameters on the properties and morphology of molybdenum carbide nanoparticle, as well as their impact on the catalytic activity. Critical issues such as structural diversity, surface properties, and multiscale reaction modeling are also discussed for better understanding of the reaction mechanism. This is a promising strategy towards synthesis of cost-effective and efficient catalysts for renewable and sustainable energy production.

1. Introduction

One of the most important research gaps in the field of renewable and sustainable energy is rational design and synthesis of suitable eco-friendly and cost-effective catalysts with preserved energy and chemical functionality for prolonged applications in several industrial processes [1–3]. The unique chemical and physical properties of molybdenum carbide nanoparticle [4] have enhanced its popularity in the fields of materials and chemical science towards production of renewable and sustainable energy [5]. The outstanding properties of MCN include thermal stability, high electrical conductivity, adsorption capacity, high melting point, and hardness [6]. Moreover, the characteristics of MCNs such as resistance to nitrogen and sulfur, high catalytic current density, and durability are similar to those of noble metals, which enable their utilization in hydrogenation and hydrogen evolution reactions (HER) [7,8]. Examples of these reactions include CO_2 hydrogenation to alcohol, CO hydrogenation to alcohol [9], hydrodeoxygenation [10], electrocatalytic hydrogen evolution from water splitting [11] including oxygen evolution reaction [12], hydro-treating [13], watergas shift reaction (WGS) [14], hydrodesulfurization (HDS) [15], CH_4 aromatization [16], and hydrodenitrogenation (HDN) [17]. The MCNs are also suitable for electrocatalytic reactions.

MCN has been used successfully to hydrogenate feedstock such as cellulose, indole, toluene, and cumene, which are popularly processed with group 9 and 10 noble metals (Pt, Pd, Rh) [18–20]. These being commercially available catalysts for reactions such as methane reforming, hydrocarbon isomerization, water-gas shift reactions, and CO hydrogenation. Further, MCN has been employed as an alternative to Ru, and to an extent Pt as electrocatalysts in the anode of polymer membrane fuel cells (PEMFC) [21–23] because of its platinum-like behaviors [24]. The thermal stability of MCN in the absence of oxygen is due to the delay of the sintering and attrition effects as reaction proceeds. However, the catalytic activity of MCN systems mainly depends on the nature and physiochemical properties of the catalyst.

Previously, the high temperature classical metallurgical process was used to prepare metal carbides but the products exhibit low specific surface areas and high particle size [25]. This results in the Metal carbide products exhibiting low catalytic performance in targeted catalytic processes [3]. Currently, the MCN synthesis method by Lee et al. [26], which is a temperature program reduction (TPR) carburization is most popular due to its remarkable improvement on the textural property of the product [27]. TPR carburization is a carbothermal reduction method that carburizes the Mo precursor supported on carbon in hydrogen atmosphere [28]. The Mo precursor is to be thermally treated, at increasing the controlled temperature in a reducing environment [29]. To form the carbide phase, the carbon source is mainly

* Corresponding author.
E-mail addresses: adeniyipee@live.com, peter.alaba@covenantuniversity.edu.ng (P.A. Alaba).

https://doi.org/10.1016/j.rser.2018.03.106
Received 25 March 2017; Received in revised form 20 March 2018; Accepted 31 March 2018

Nomenclature

CVD	Chemical vapor deposition
DFT	Density functional theory
DFTB	Density functional tight-binding
EAM	Embedded atom type
ELM	Extreme learning machine
Fcc	Face-centered cubic
Hcp	Hexagonal closest-packed
HDN	Hydrodenitrogenation
HDS	Hydrodesulfurization
HER	Hydrogen evolution reactions
IMLS	Interpolating moving least squares
JCPDS	Joint Committee on Power Diffraction Standards
MCN	Molybdenum carbide nanoparticle
MM	Molecular mechanical
MSI	Modified Sheppard interpolation
NN	Neural-network
PES	Potential energy surface
QM	Quantum mechanical
RKHS	Kernel Hilbert space
RPBE	Revised Perdew–Burke–Ernzerhof
RT	Room temperature
t_{carb}	Carburization time
T_{carb}	Carburization temperature
TMC	Transition metal carbides
TPH	Temperature-programmed hydrogenation
TPR	Temperature program reduction
US	Umbrella sampling
WGS	Watergas shift reaction

light hydrocarbon, while hydrogen is the reducing agent. The essence of the controlled temperature is to optimize the carburation temperature to avoid sintering of the reduced Mo particles, thereby reducing the particle size of the resulting carbide. The carburization conditions (temperature and time) control the physiochemical properties, the chemical nature, and structure of the resulting carbide phase. MCN exists in two main crystalline structures: orthorhombic and hexagonal (Mo_2C) and hexagonal structure. The preparation methods of carbide-supported metal catalysts include wet impregnation [30], atomic layer deposition [31] and vacuum environment [32]. Mostly, the synthesized MCN, passivated prior to its exposure to air to prevent oxidation.

The goal of this review is to provide insight into the surface properties of MCN and its reaction mechanism for renewable and sustainable energy production towards a sustainable future. In Section 2, rational design and synthesis of MCN are discussed, highlighting the effect of operating parameters. The third section deals with a structural diversity of MCN using density functional theory (DFT) to categorize different form of MCN based on structural differences. Section 4 briefly discusses the surface properties of MCNs to determine the stability based on their structural diversity. While Section 5 gives an insight into multiscale reaction model on MCNs for a better understanding of catalytic reaction mechanism of the system, which is crucial to the commercial applications of MCN in the production of renewable and sustainable energy. Finally, we presented the catalytic activity of MCN based catalysts (both unsupported and promoted/supported) in Section 6.

2. Preparation of MCN

MCNs are popularly prepared by carbothermal reduction carburization process. This process consists of three different steps; (i) deposition of the Mo-precursor on the carbon source, (ii) carbothermal reduction of the Mo-precursor to produce MCN, and [33] the subsequent stabilization of the produced MCN by Mo-carbide surface passivation [19]. Generally, synthesis of MoO_2 nanoparticles is not a difficult task; the transformation into MCN is where the major challenge is. The transformation is so complex due to the influence of several variables. Experimentally, different kind of MCN is prepared using various strategies. These strategies include direct carburization of MoO_3 by 10–20% CH_4–H_2 mixtures at 750 °C for 4 h to produce thermodynamically stable hexagonal Mo_2C [34]; reduction of MoO_3 by NH_3 to produce Mo_2N and then carburization of Mo_2N by using CH_4–H_2 mixture to produce orthorhombic Mo_2C [35] reduction and carburization of belt-shaped α-MoO_3 by using 5% *n*-C_4H_{10}–H_2 mixture at 700 °C for 4 h to produce metastable phase face-centered cubic (fcc) α-MoC_{1-x} [36]; solid-state reaction in combination with H_2 reduction at 800z °C to form hexagonal Mo_2C at 20 min reduction time and hexagonal η-MoC at 10 min reduction time using glucose as the carbon source [37]. However, carburization with a 10% C_2H_6–H_2 mixture produces in mixed crystal phases [36]. All the phases can be differentiated and identified with ease. MCN can also be synthesized via reactive hard-templating, a technique where a precursor such as $MoCl_5$ is used with mpg-C_3N_4 as a template in ratio 1:1 in ethanol solution (Eq. (1)) [38].

$$(MoCl_5 + 2C_2H_5OH \rightarrow MoCl_3(OC_2H_5)_2 + 2HCl) \quad (1)$$

Furthermore, Hare et al. [39] and Saito et al., [40] used arc discharge method to prepared β -Mo_2C and α-Mo_2C encapsulated with polyaromatic carbon. The most efficient and common strategy for MCN production is high temperatures reduction and carburization of MoO_3 by a mixture of hydrocarbon and hydrogen. The major advantages of this strategy are the formation of a pure crystal phase and avoidance of contamination by coke. Typically, the crystalline phase can be controlled by reconciling the gas composition of the reducing and carburizing agent [41]. However, the effect of the operating parameters has not been significantly explored. The synthesized MCN normally possess random size distribution, which ranges from few nanometers to several hundred nanometers with irregular shapes [42].

2.1. Effect of operating parameters on the nature of MCN

The effect of carburization conditions such as carbon source, pretreatment temperature T_{preT}, heating rate, Mo loading, carburization time (t_{carb}), carburization temperature (T_{carb}), Mo-precursor and crystalline phases is vital on the MNC crystalline Mo-phases. The effect could be analyzed by comparing the measured H_2-consumption from TPR results and the crystallinity of the carburized samples via XRD analysis.

2.1.1. Carbon source

The morphology of MCN is highly sensitive to the choice of hydrocarbon used. Mo et al. [43] reported that a high concentration of carbon source such as long chain hydrocarbon favors the formation of MoC (with face-centered cubic (fcc)) and nanosized Mo_2C (with hexagonal closest-packed (hcp)) due to the severity of carbon deposition at high carburization temperature. The deposited carbon may block the mesopores to form new micropores [43]. Further, increasing the chain length of the carbon source lessens the particle size and the required carburization temperature for MCN synthesis [41]. The use of low concentration of small chain hydrocarbon leads to agglomeration of carbide particles at a low heating rate. Prominent among the carbon sources are 20% CH_4–H_2 to form hexagonal close-packed MCN, 5% n-C_4H_{10}–H_2 to form fcc MCN, 10% C_2H_6–H_2 to form mixed crystal phases by the reducing and carburizing the precursor. The MCN synthesized with C_2H_6–H_2 as the carburizing agent exhibits the roughest surface and highest adsorption capacity for H_2, while synthesized with n-C_4H_{10}–H_2 exhibits a very condensed surface [41]. Recently, Tang et al. [37]

explored the use of glucose as a cheap and environmentally benign carbon source. They successfully produced MCN with a high surface area by using a facile solid-state reaction together with H_2 reduction at 800 °C.

2.1.2. Pre-treatment temperature

The influence of pre-treatment temperature plays a vital role in carburation and crystallinity of MCN. Ma et al. [44] revealed that pre-treating the precursors helps to achieve a complete carburization at a lower temperature compared to unpretreated samples. Guil-Lopez et al. [19] studied the effect of pre-treatment temperature on MCN obtained at 10% Mo loading, 710 °C T_{carb}, and t_{carb} of 60 min in an argon stream. Two different T_{preT} 250 and 550 °C were used to produce samples E-11 and E-12 respectively. The TPR-H_2 consumption profile showed that sample E-11 exhibited two different sharp peaks. A low-temperature peak and an incomplete high-temperature peak (Fig. 1a), which indicates incomplete carburization. Meanwhile, sample E-12 has no sharp peak at low temperature because Mo^{6+} completely reduced to Mo^{4+} as the pretreatment proceeds at 550 °C. Moreover, the unfinished carburization of sample E-11 is mainly because its carburization commenced at a temperature (635 °C) higher than that of E-12 (600 °C).

Further, the unfinished carburization of E-11 lead to the formation of a large amount of crystalline MoO_2 phase rather than MCN as presented in the samples XRD pattern (Fig. 1b). A few traces of MCN and graphite, which corresponds to the carbon source were also present. However, the XRD pattern of sample E-12 shows that the sample is predominantly MCN with a trace of graphite due to complete carburization of the precursor. Therefore, low-temperature pretreatment speeds up the carburization reaction of Mo° rather than a reduction of MoO_2.

2.1.3. Heating rate

Guil-Lopez et al. [15] investigated the effect of heating rate on the formation of MCN at 20% Mo loading, T_{carb} = 840 °C, and t_{carb} = 5 min in an argon stream. Two different types of carburation experiments were used to produce sample E-2 and E-10 respectively. The first carburation was done at 10 °C/min till the T_{carb} from room temperature (RT) while maintaining t_{carb}. The second type was conducted at 10 °C/min till 550 °C and successively heated at 3 °C/min from 550 °C to T_{carb}. The TPR-H_2 consumption profile shows that both samples have two complete different sharp peaks. A low-temperature peak and a high-temperature peak (Fig. 2a). Moreover, the carburization of sample E-10 commences at a temperature (575 °C) earlier compared to that of E-2 (618 °C) and the peak temperatures are 693 and 760 °C (Fig. 2a). This shows that the carburation of the sample is favored by low heating rate [29] as in E-10. From the XRD pattern (Fig. 2b), it is vivid that both samples are majorly MCN with a trace of graphite from the carbon source. However, E-10 exhibits higher MCN particle size than E-2 due to sintering of the carbide phase of the sample, induced by high temperature.

2.1.4. Carburization temperature

One of the major requirement for synthesis of MCN, which makes it difficult to reproduce and control the desired particle size and surface area is high temperatures [34]. Guil-Lopez et al. [15] did an extensive study on the effect carburation temperature on the crystalline phases of MCN at 50% Mo loading, 250 °C T_{preT} and t_{carb} of 5 min using heating of 10 °C/min in an argon stream. The samples were carburated at four different T_{carb} = 500, 650, 700 and 840 °C to form sample E-6, E-7, E-8 and E-1 respectively (Fig. 3). All the samples exhibit only one peak at low temperature except E-1 that has another incomplete peak at high temperature. Further, the low-temperature peak of E-6 is incomplete, while it terminated at about T = 600 °C for E-7, and E-8. This indicates that samples E-6, E-7, and E-8 are mainly MoO_2 with a trace of Mo° for sample E-8, while E-1 comprises of MCN, Mo°, and MoO_2. The presence of MoO_2 and Mo° in E-1 is due to incomplete carburization at the high-temperature peak. The XRD patterns of the samples also confirm the composition of the samples (Fig. 3b). The incomplete carburization of E-1 is because of insufficient carburization time. However, several researchers like Guzmán et al. [34], Xiao et al. [41], Mo et al. [43] were able to achieve complete carburization at low temperature but at a reasonable length of time. Therefore, it is tenable to adduce that low-temperature carburization is visible at a reasonable length of carburization time. This claim is well proven in the next subsection.

2.1.5. Carburization time (t_{carb})

Fine-tuning t_{carb} with other parameters like T_{carb} is crucial towards achieving a completely carburized MCN phase [34]. The study of Guil-Lopez et al. [15] investigates the effect of t_{carb} on the carburation and crystallinity of MCN. The samples pre-treated at 200 °C containing 50 wt% Mo was carburated using heating rate of 10 °C/min to 840 °C at a different time of 5 and 60 min for samples E-1 and E-9 respectively (Fig. 4). Fig. 4a shows that 5 min carburation (E-1) exhibits an incomplete carburation, while the carburation was completed for E-9. Therefore, a long t_{carb} is essential for a complete carburation at 840 °C due to low carburation rate. The composition of the two samples is vivid in Fig. 4b. Sample E-1 comprises of crystalline phases of MCN, MoO_2, and Mo^0 while E-9 is purely MCN crystalline phase. The presence of MoO_2 and Mo^0 in E-1 is due to the incomplete carburization.

2.1.6. Carbon/metal ratio

Carbon/metal ratio plays a vital role in the design of MCN due to its remarkable impact on the chemical and catalytic properties. The increase in carbon/metal ratio leads to a decrease in adsorption energy but an increase in the dissociation barrier. The study of Posada-Perez et al. [45], shows that an increase in the carbon content of MCN from Mo_2C to MoC lessens the reactivity of the Mo centers because the MoC surface is saturated and less metallic, while that of Mo_2C is unsaturated and more metallic [46]. Although, the Mo centers are still capable of binding CO_2 molecule effectively without breakage of the second C–O bond, the cleavage of the first C–O bond need to be supported by hydrogen as shown below [47]:

$$H + OCO \rightarrow HOCO \rightarrow HO + CO \quad (2)$$

Consequently, MoC is a selective catalyst for reduction of CO_2 to CH_3OH. The remarkable impact of carbon/metal ratio on catalytic and chemical properties of MCN is illustrated in Fig. 5.

The rate of production of CH_3OH increases as the ratio increases from Mo_2C to MoC making MoC a better catalyst for the system.

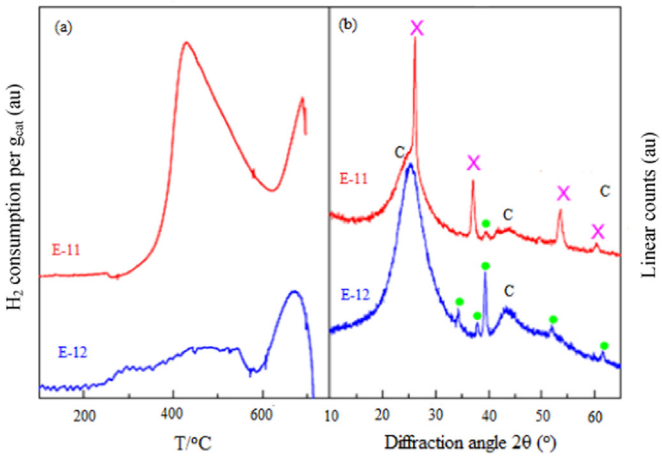

Fig. 1. The effect of the argon pretreatment on the nature of MCN. Illustrating (a) TPR-H2 profile in the course of the carburization process, and (b) XRD pattern showing the crystalline phases of the synthesized MCN. Recognized crystalline phase: (●) Mo_2C, (X) MoO_2, and the support (C); adopted from [20].

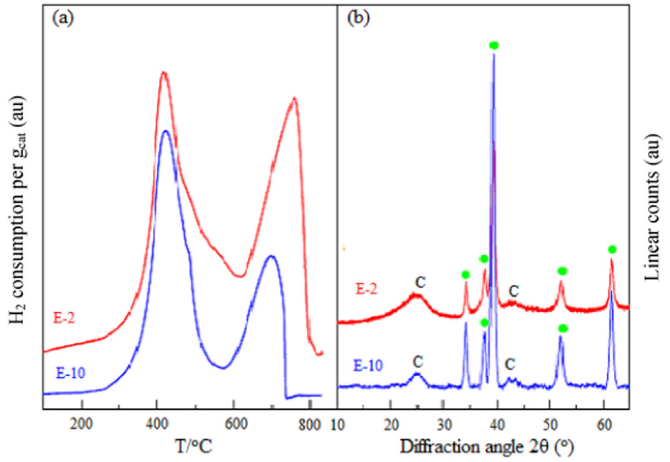

Fig. 2. Effect of heating rate during carburization on the nature of Mo-materials. Illustrating (a) TPR-H2 profile in the course of the carburization process, and (b) XRD pattern showing the crystalline phases of the synthesized MCN. Recognized crystalline phase: (●) Mo_2C, and the support(C); adopted from [20].

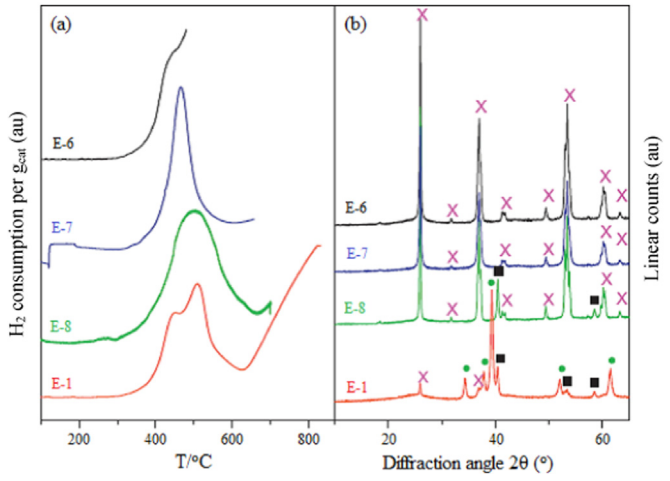

Fig. 3. Effect of the maximum carburization temperature (Tcarb) on the nature of Mo-materials. Illustrating (a) TPR-H2 profile in the course of the carburization process, and (b) XRD pattern showing the crystalline phases of the synthesized MCN. Recognized crystalline phase: (●) Mo_2C, (■) Mo, and (X) MoO_2; adopted from [20].

Therefore, MoC is a viable and selective catalyst for high temperatures synthesis of CH_3OH.

2.2. Surface carbon species

The surface carbon species [48] of MCN comprises of free carbon, adsorptive carbon, and carbidic carbon. The free carbon could be pyrolytic or graphitic carbon, left on the MCN surface during high-temperature hydrocarbon degradation. Graphitic carbon exhibits a higher graphitization degree than the pyrolytic carbon [49,50]. The adsorptive carbon is the weakly adsorbed matter for instance bonded molecules of CO and CO_2 [51]. The carbidic carbon is the native carbon, which could be carbon-terminated Mo_2C and the strong adsorptive CS like the one attributed to disassociation of adsorbed feedstock. The report of Mo et al. [43] indicates that the graphitic carbidic, adsorptive, and pyrolytic were in the range of 200–300, 460–490, 600–690 and 700–800 °C, respectively on MCN surface based on temperature-programmed hydrogenation (TPH) (Fig. 6).

3. Structural diversity of molybdenum carbide

Understanding the structural diversity of MCN is an uphill task due to its complex nature and a number of metastable and stable phases [52]. However, density functional theory (DFT) based estimations with the revised Perdew–Burke–Ernzerhof (RPBE) exchange-correlation functional has been successfully employed to identify the crystal structure [53]. MCN is characterized by five different crystal structures: α-MoC_{1-x}, α-Mo_2C, β-Mo_2C, γ-MoC and η-MoC [54], which arise from different preparation methods as well as carburizing agents [55]. The composition and dispersion of Mo and C in the structures vary influencing the electrochemical activity. Further, the structures exhibit varying sizes of the tunnel, which affects ions insertion. The crystal structure of α-MoC_{1-x} is fcc, which is similar to that of NaCl while both γ-MoC and η-MoC exhibit hexagonal structures but different stacking sequence [54]. According to the Joint Committee on Power Diffraction Standards (JCPDS) data files, β-Mo_2C is orthorhombic with the Mo arrangement slightly distorted from hcp [51], while α-Mo_2C has hcp surface with carbon atoms incorporated at the octahedral interstitial sites [55]. Both of them are suitable for hydrogenation of CO [5,56] and conversion of benzene to cyclohexane [57]. However, the orthorhombic β-Mo_2C is more stable while the hexagonal α-Mo_2C is less stable [58]. Fig. 7 presents the Bulk crystallographic structures of MCN.

Prominent of all the MCN structures are α-MoC_{1-x} [59] and β-Mo_2C [24,60] due to their high stability and remarkable electrochemical performance, which is attributable to their large ionic contribution [55]. Further, β-Mo_2C is a suitable electrocatalytic material due to its low work function (3.4 eV), which facilitates surface-adsorbate electron transfer [55]. Based on DFT computation, β-Mo_2C exhibits a stronger metallic property than the other polymorphs, which show the strongest covalent bond [55]. The lattice constant computed using DFT-RPBE for bulk α-MoC_{1-x} is 4.36 Å [61,62] while the experimental value is 4.33 Å [63]. The β-Mo_2C comprises a sequence of alternating Mo and C layers with DFT-RPBE lattice constants: a = 4.819 Å, b = 6.012 Å, and c = 5.150 Å [61,62], which are similar to the obtained experimental data by [64]. The lattice constant of computed for α-Mo_2C are: a = b = 6.118 Å and c = 4.682 Å [46], which are reportedly close to the experimental values [65]. All the strategies for MCN preparation are related to reductive carburization of the precursor material in a stream containing hydrogen via TPH [66], and chemical vapor deposition (CVD) [67], liquid-phase reaction [68], template method [69], etc. Prominent of all the strategies is TPH, which involves a reductive reaction between the hydrogen, carbon source (light hydrocarbon) and the Mo precursor. To obtain β-Mo_2C with an enhanced number of active sites, *in situ* carburization is vital. This constructs β-Mo_2C nanoparticles with a fast electron transfer path, which could be covalently anchored on a promoter [70]. The reaction scheme is given in Fig. 8.

Due to all these outstanding qualities of MCNs, β-Mo_2C was proposed as a viable substitute for the conventional Cu-based catalysts utilized in reactions like Water-Gas-Shift (WGS) [71,72] while α- Mo_2C highly suitable for dehydrogenation of ammonia [73].

4. Surface properties of MCNs

MCNs possess a similar surface to that of transition metal surface M (111), which is a little more reactive toward $CH_{2/3}$ species when compared with metals with a similar strength of carbon adsorption. This makes MCN a suitable for hydrogenation reaction, which is less vulnerable to graphite poisoning because of an increased attraction to hydrocarbons [74]. Moreover, Mo_2C (001) has a similar the O/OHx binding with that of the transition metal M(211) surfaces indicating the likelihood of oxygen poisoning on Mo_2C surfaces. However, if there is deposition of oxygen from the decomposition of CO_2 or water, the Mo_2C surface becomes stable against subsurface oxidation, while for oxygen deposition from methanation of CO, a subsurface oxycarbide is

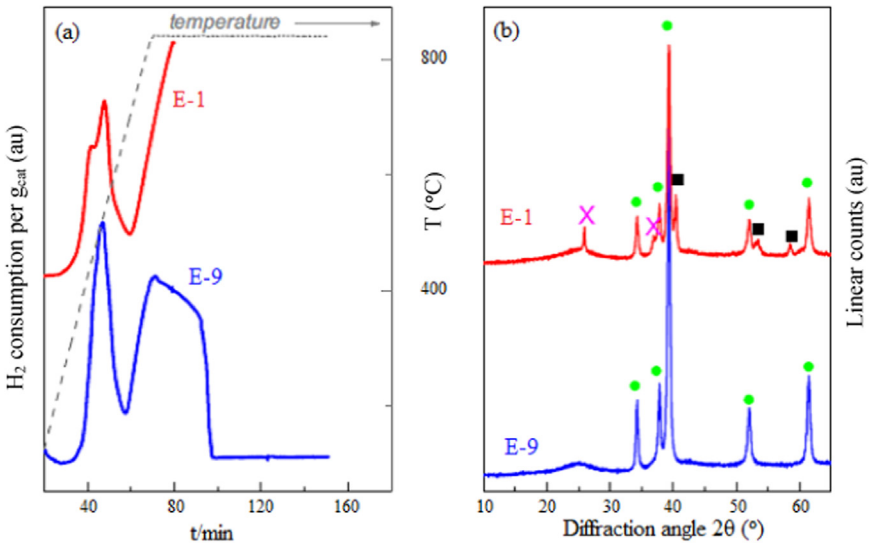

Fig. 4. Influence of the time (tcarb) at maximum carburization temperature (Tcarb) on the nature of Mo-materials. Illustrating (a) TPR-H2 profile in the course of the carburization process, and (b) XRD pattern showing the crystalline phases of the synthesized MCN. Recognized crystalline phase: (●) Mo_2C, Mo, and (X) MoO_2; adopted from [20].

expected to be stable at low temperatures and lower kinetic rate as compared with carbon dioxide or water decomposition [74]. The suitability of MCNs for hydrogenation reaction is also supported by the outcome of the study of Posada-Perez et al. [45], which concluded that MCN is an active and selective catalyst for CO_2 reduction to methanol. This is because adsorption and decomposition of CO_2 are more effective on the surface of Mo-terminated β-Mo_2C(001) compared to transition metal surfaces like Cu(111) being the surface that is generally used as a standard in catalysis [75]. Posada-Perez et al. [45] stated that the apparent activation energy obtained for the synthesis of CH_3OH via CO_2 reduction on MoC is 17.2 kcal mol^{-1}, which is lower than the respective values of 25.4 and 20.9 kcal mol^{-1} reported for Cu(111) and TiC(001) [76].

Several studies show that the structure of Mo_2C surface depends on the annealing time and temperature [77–80]. The study of Lo et al. [77] reveals that the three-fold hollow sites of Mo layer were occupied by the C atoms when annealed below 687 °C when high-resolution images of Mo_2C(0001)-($\sqrt{3}\times\sqrt{3}$)R30° structure were investigated by scanning tunneling microscopy. Fig. 9 presents the low Miller-index surfaces of fcc α-MoC_{1-x}, hexagonal MoC, α -Mo_2C and β-Mo_2C. The α-MoC_{1-x}, exhibits (001), (011) and Mo- and C-terminated (111) polar surfaces. The (001) surface is found to be the most stable while (011) surface is unstable. The hexagonal MoC phase, which is obtained with an annealing temperature of 1327 °C [79] possesses (001) and (100) polar surfaces with both Mo- and C-termination (Fig. 10).

Both α -Mo_2C and β-Mo_2C have Mo- and C-terminated polar surfaces ((001) and (111)) when annealed above 1027 °C and nonpolar (100), (011), and (101) [78]. The atomic sites were completely relaxed in all the slab super-cell models even though neither the variations in surface energies nor the surface reconstruction was amongst the engaged super-cells [55].

The surface stability of MCNs are not only determined by the surface structures but also operating conditions like carburization condition during its preparation, which also affects the surface structures. The surface structure influences the surface energy, which has a close relationship with the value of carbon chemical potentials (μ_C). The study of Wang et al. [81] shows that different surface terminations give different trends with μ_C. This means that the surface energies of Mo terminations increase as μ_C increases, while those of C terminations decrease, indicating that Cterminated surfaces are more stable under stronger carburization capacity large value of μC than Moterminated polar surfaces. The most stable surface varies with μC. For instance, (1 1 0)Mo termination exhibits the best stability within the range of − 12.0 to − 10.7 eV value of μ_C, while the (1 0 0)Mo termination exhibits the best stability within the range of − 10.7 to − 10.2 eV. Within the range of − 10.2 to − 9.5 eV, the (1 1 1)Mo/C1 termination shows the best stability. Within the range of − 9.5 to − 8.5 eV, the (1 1 0)Mo/C2 termination becomes the best based on stability, while the (1 1 0)Mo/Crelaxed termination exhibits the best stability within the range of − 8.5 to − 6.0 eV. This is a clear indication that the choice of surfaces, as well as terminations, is essential towards a better understanding of important catalysis reaction mechanisms via DFT computations.

5. Multiscale reaction model on MCNs

For a better understanding of catalytic reaction mechanism with MCNs, there is a need to establish a multiscale reaction model, which combines quantum mechanical (QM) density functional tight-binding (DFTB) technique with a molecular mechanical (MM) force field [82,83]. This could be accomplished by building a QM/MM model to define the MCN, the model aromatic solvent, and the surroundings. The free energy profiles of the reactions could be determined by using Umbrella sampling (US) [82]. Liu and Salahub [82] studied a multiscale reaction model of a catalytic hydrogenation of benzene on MCN by using QM/MM method together with US technique towards *in situ* upgrading of heavy oil. Their report shows that the multiscale model reveals new features of MCN as compared with the traditional computational method. Consequently, the MCN and the solvent made entropic contributions, which significantly influence the free energy profiles of the nanoscale heterogeneous reactions to establish a reaction working condition. Fig. 9 gives the optimized embedded reactant state of the first hydrogenation reaction.

However, the multiscale model efficiency is determined by the cost of computation on ab initio. It is of vital importance to search for a more economical means for large-scale simulation using ab initio molecular dynamics [84]. Functional forms such as bond-order based potentials suggested by Brenner and Garrison [85] and Tersoff [86] for covalent materials, embedded atom type (EAM) potentials for metals [87], and classical force fields [88] for molecular systems has been recommended. However, they are all limited in numerical accuracy and inability to reuse the functional form for another system order than the particular system for which it was modeled [89]. Further, several approaches based on electronic data fitting such as splines [90], Gaussian approximation potentials [91], modified Sheppard interpolation (MSI) based on a Taylor expansion [92], genetic programming [93], reproducing kernel Hilbert space (RKHS) [94], expansion in terms of invariant polynomials (IP) [95] and interpolating moving least squares (IMLS) [96] have been suggested. Although these approaches are

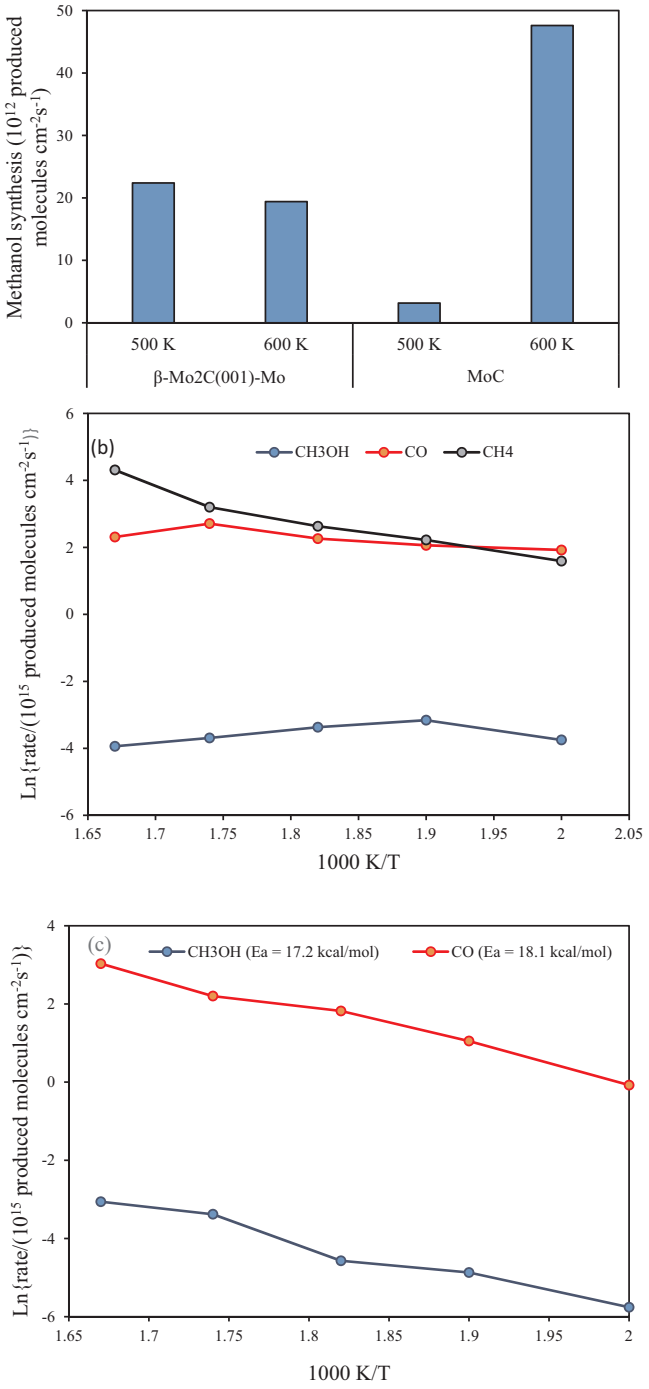

Fig. 5. (a) Production rates of methanol from CO_2 hydrogenation on β-Mo_2C(001)-Mo and polycrystalline MoC at 500 and 600 K and Arrhenius plots for the production of (b) CO, methane and methanol on β -Mo_2C(001)-Mo; (c) CO and methanol on MoC at temperatures of 600, 575, 550, 525, and 500 K. In a batch reactor, the metal carbide catalyst operating at 0.049 MPa (0.5 atm) of CO_2 and 0.441 MPa (4.5 atm) of H_2; adopted from [48].

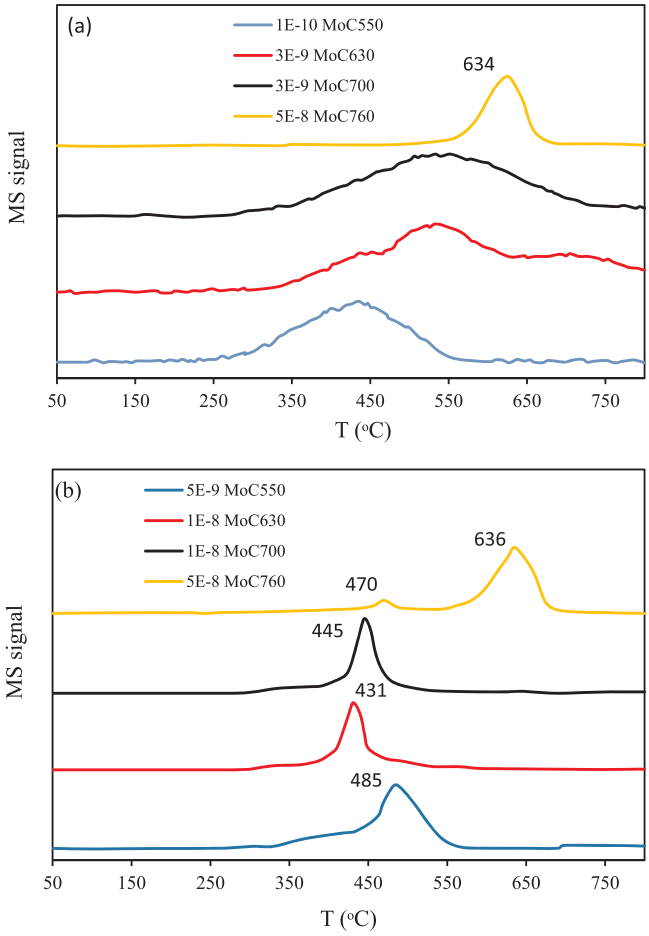

Fig. 6. TPH profiles of the MCN before (A) and after (B) CO hydrogenation reaction at m/z = 15 adopted from [39].

exceptionally and perfectly numerical, the functional form is "non-physical" (bias-free). Therefore, the construction of the PESs needs to be great carefully done to give the appropriate physical representation of the system [89].

Recently, the use of neural-network (NN) as an intelligence technique to represent the ab initio potential energy surface (PES) adaptively is a promising approach. NN offers a remarkable computational efficiency and is capable of reproducing the experimental data thereby giving an exceptionally cheap and quality model of the physicochemical process [97]. Neural-network is a class of algorithms formulated for various applications [89]. Among them are applications related to PES such as estimation of the correlation energy of heavy atoms and diatomic molecules [98], modeling of bond energies [99], enhanced enthalpies [100,101] and heat of formation [102], and lower level electronic structure-based computation of DFT energies [103]. The applications ride on the capability of NNs to discover a hidden pattern in complex data [89]. According to the study of Behler [89], NNs offer several advantages compared to the conventional potential. The advantages include accuracy, improvability, efficiency, cost-effectiveness, lack of system specific terms, the ability to deal with high dimensional PESs and ability to analyze how bonds are broken and made. Furthermore, the construction is highly automatic with little human effort. The potential constructed for a specific system can be used to predict the energies of atomic configurations of related structures in the training set. In addition, the analytic gradients are readily available due to their well-defined functional form. The recent study of Artrith and Behler [104] on the properties of bulk copper and of a variety of surface structures reveals that NN PESs have the capacity to produce a similar result with that DFT at a small fraction of the computational costs.

NN PESs could be constructed via several approaches, which include single NN, systematic NN potentials, and high-dimensional NN potentials. Single NN PESs can be trained implemented with ease and the potentials could be evaluated speedily and accurately. However, they are only applicable to small molecules because the potentials are limited to low degree of freedom. PESs based on systematic NN potentials are suitable for large molecule [105,106] and serve as an intermediate to high-dimensional NN potentials. High-dimensional NNs normally

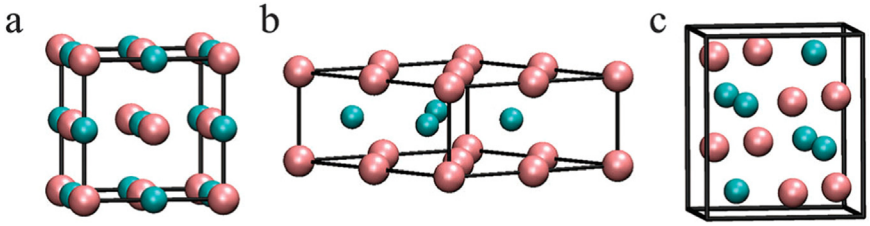

Fig. 7. Bulk crystallographic structures of (a) fcc α-MoC_{1-x}, (b) hexagonal γ-MoC and η-MoC, and (c) orthorhombic β-Mo_2C. Turquoise and magenta spheres denote C and Mo atoms, respectively adopted from [57].

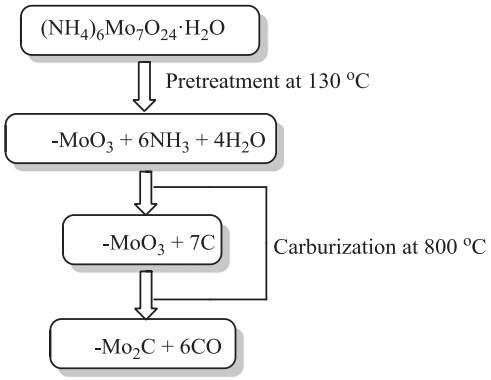

Fig. 8. Reaction scheme for Mo2C formation via *in situ* carburization using Temperature program hydrogen (TPH).

suitable for huge systems comprising some thousands of atoms [89]. According to the study of Behler [89], an ideal potential should be high-dimensional and obviously determined by using the entire degree of freedom of the system with a reliable set of high-level ab initio data. It could be used for a variety of systems without changes in their functional form, and a remarkable accuracy close to the fundamental first-principles molecular dynamics simulations is achievable because of their bias-free construction [107,108]. Sosso et al., [109] even suggested that the capability of NN PES is beyond that of the first-principles. This was observed when they used NN techniques to develop a classical interatomic potential for the bulk phases of GeTe.

However, high-dimensional NN potential is more costly. They are capable of providing energies and forces from 100 to 200 atoms per second per computation core on average desktop computers, although it is by far faster than DFT [110]. Since NN PESs need bigger training sets compared to other kinds of potentials for an adequate description of the physics of the system, it is mandatory to consider the required equilibrium structures as well as non-stationary points in the training set to avoid holes in high-dimensional NN PESs. However, the training data set should be minimized to reduce computational cost, since only the energetically reachable part of the data set such as the configurations visited in MD simulations are significant [89].

Shen et al. [83] studied a multiscale model towards lowering the cost of ab initio computation by using NN as proposed by Behler and Parrinello [110]. They developed a semi-empirical QM/MM model for determination of potential energy of a specific QM/MM system at ab initio QM/MM level. The developed model was further utilized for three more reactions in water to estimate the changes in free-energy. The ab initio QM/MM level was obtained by converting the semi empirical QM/MM model computed free-energy profile with the potential energies predicted with the developed NN. The obtained results show a remarkable correlation with the reference data gotten from the ab initio QM/MM molecular dynamics model [83]. This shows that application of NN method couple with semiempirical QM/MM model is an efficient and reliable approach for modeling of a chemical reaction. The previous study of Nguyen-Truong et al. [111] also attested to the efficacy of NN by using Levenberg–Marquardt (LM). They revealed that the algorithm is exhibited high accurate with less training iterations and the fitting (vibrational PES of H_2O, reactive PESs of O_3 and ClOOCl) require fewer data points.

However, the use of NN is becoming an old fashion due to the emergence of a simpler, more cost-sensitive and efficient learning approach known as extreme learning machine (ELM) developed by Huang et al. [112]. This is because ELM exhibits extremely fast learning speed, superior suitability for high-dimensional potentials, and generalization capability. ELM is a learning algorithm for single-hidden layer feed-forward neural networks (SLFNs), which selects hidden nodes randomly and computes the output weights of SLFNs analytically. ELM can be regarded as a linear system after the input weights and the hidden layer

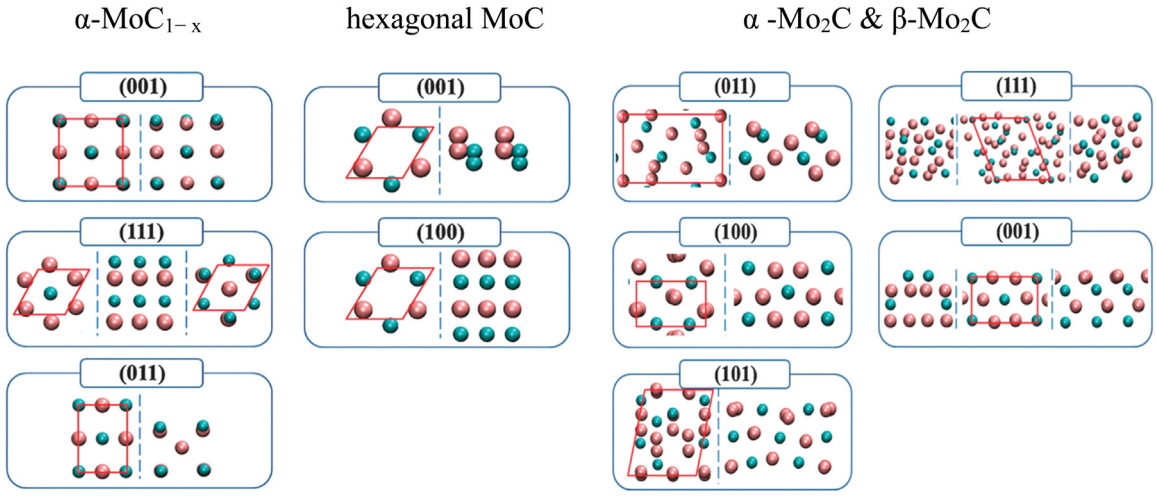

Fig. 9. Top (left panels) and side views (right or middle panels) of the considered α-MoC_{1-x}, hexagonal MoC, and α -Mo_2C & β-Mo_2C surfaces. In the α-MoC_{1-x} (111) surfaces three panels are presented, being Mo- (left panel) and C-terminations (right panel). On α -Mo_2C & β-Mo_2C polar surfaces—(111) and (001)—left and right panels belong to C- and Mo-terminations whereas the middle panel is a top view. Surface unit cells are appeared as red lines; adopted from [57]. (For interpretation of the references to color in this figure legend, the reader is referred to the web version of this article.)

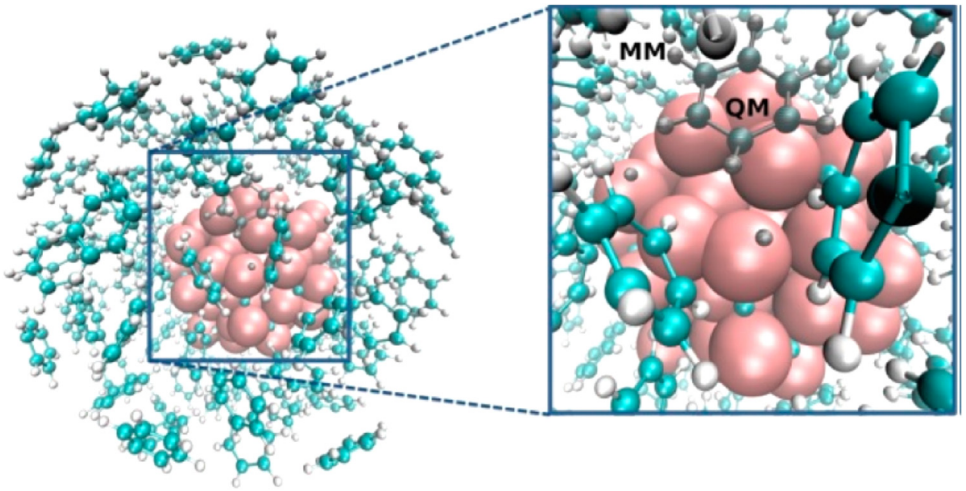

Fig. 10. QM/MM model of a 1.2nm MCN (Mo atoms in red and C atoms in cyan) with adsorbed benzene (in black) and the two dissociated H atoms (in black) embedded in the model aromatic solvent; adopted from [84]. (For interpretation of the references to color in this figure legend, the reader is referred to the web version of this article.)

biases are randomly selected [113]. Being one of the foremost trends for optimization and high learning speed in the machine intelligence community, ELM has a promising potential to scale up for several practical applications, while attaining the developments in theories, applications, and hardware implementation [113,114].

By using ELM, the neural networks training time can be lessened by a thousand times. The performance of ELM has been assessed on several benchmark problems [115]. However, ELM PESs not been investigated to the best of our knowledge.

6. Application of MCN for hydrogenation and hydrogen production

6.1. Unsupported MCN

Recently, Posada-Pérez et al. [116] reported the use of MCN heterogeneously catalyzed hydrogenation reactions, where H_2 is adsorbed and dissociated. The study was carried out using systemic DFT-PBE with or without dispersion terms, regarding the interaction and stability of H_2 with orthorhombic β-Mo_2C(001) and cubic δ-MoC(001) surfaces. For β-Mo_2C(001), two likely Mo or C terminations are considered. Their report shows that the energy profiles for the elementary steps H_2 dissociation are mainly influenced by dispersion. The DFT-PBE computation with vdW dispersion give an energy barrier of 0.60 eV for δ-MoC, and essentially zero on β-C and β-Mo, while it was predicted that computation with vdW would favorable desorption of δ-MoC and β-C more than dissociation. The computation of surface free energy calculations indicates that both terminations of β-Mo_2C become stable as H coverage increases. On the other hand, in the case of the δ-MoC (001) surface, adsorption of H becomes stable up to half coverage where all C sites are filled (Table 1).

Li et al. [36] developed belt-shaped MCN (α-MoC_{1-x} and β-Mo_2C) for dehydrogenation of benzyl alcohol to benzaldehyde. Their report shows that β-Mo_2C nanobelts displayed a higher catalytic performance than the α-MoC_{1-x}. The outstanding performance of β-Mo_2C could be attributed to the high number of coordinatively unsaturated Mo sites on its surface. The study of T. Mo et al. [43] on hydrogenation of CO, states that increase in the degree of carburization weakens the CO adsorption strength on MCN. However, increase in degree carburization of MCN engenders a continuous increase in the intrinsic activity with respect to TOF. Table 2 presents the catalytic performance of various unsupported MCN catalysts.

6.2. Supported MCN

Several authors have studied supported MCN for the purpose of establishing selectivity control in reactions such as HDO. Boullosa-Eiras et al. [120] studied the use of TiO_2 supported MCN (Mo_2C/TiO_2) as an alternative catalyst for HDO of fast pyrolysis of phenol as a bio-oil model compound. The reaction was performed at a temperature range of 350–450 °C at a pressure of 25 bar. The primary product obtained is benzene (large amount) via hydrogenolysis, indicating high selectivity towards benzene. Small quantities of non-aromatics such as methylcyclopentane, cyclohexene, and cyclohexane were also observed. The best catalytic performance was obtained at 350 °C and 25 bar with a moderate deactivation after 9 h on stream.

MCN supported platinum (Pt/Mo_2C) catalysts was successfully used for water gas shift (WGS) reaction, exhibiting a remarkable WGS rate (mol CO/mol_{Pt} s), which is better than the rates reported for commercial Cu-Zn-Al catalyst and most of the active oxide supported Pt catalysts (like Pt/CeO_2, Pt/CeO_x, and Pt/TiO_2) [117].

Zou et al. [122] investigated the effect of various additives such as K, Ce, Co, Mg and La on MCN supported on Ni impregnated γ-Al_2O_3 during tri-reforming of methane. Their report shows that the presence of Ni species stirred-up methane dissociation and made active carbon available for the carburization process. Addition of La to the Ni supported MCN is capable of preventing small particles aggregation, facilitating topotactic transformation of MCN species and suppressed deposition of carbon, thereby leading to remarkable catalytic performance. Addition of Ce and Co resulted in deterioration of the activities of the catalyst to some extent because the particle size is larger, while the addition of Mg decreased the porosity of the catalyst and promoted coke formation. The addition of K inhibited the carburization process of molybdenum oxide species and caused the phase transformation of active γ-Al_2O_3 to less active θ-Al_2O_3. K and Mg-promoted Ni supported MCN, particularly the former, displayed a dramatic decline in the redox ability for the methane tri-reforming.

Chai et al. [123] studied the effect of various carbon support (graphitic mesoporous carbon (GMC), carbon black and activated charcoal) on MCN during catalytic hydrogenation of CO to produce mixed alcohol. Their report shows that the catalytic performance of the catalysts depends on MCN particle size rather than the type of support (Table 3). Consequently, GMC was observed as the most promising support of β-Mo_2C due to its ability to form smaller carbide particles leading to higher catalytic performance. Incorporation of a small amount of K_2CO_3 into β-Mo_2C/GMC (molar K/Mo = 0.05–0.5) as a promoter considerably favors the production of C2+–OH, resulting in a maximum space time yield (STY) for C2+–OH at medium K/Mo ratio of 0.1. K_2CO_3 promoted β-Mo_2C/GMC exhibited a better C2+–OH selectivity and space-time yield (STY) when compared with a typical Rh/GMC catalyst when triply promoted with oxide of Fe, Li, and Mn.

Kiai et al. [124] prepared a series of carbon nanotubes (CNTs)

Table 1
Preparation parameters of molybdenum carbides.

Crystal phase and size (nm)	Mo-precursor	Red. agent	Carb. Agent (%–%)	T_{preT} (K)	β [a] ($K\,s^{-1}$)	T_{carb} (K)	t_{carb} (s)	Application	Ref.
α-Mo_2C (-)	MoO_3	Magnesium	Graphite	973	10	1373			[37]
Mo_2C (11)[b]	$(NH_4)6Mo_7O_{24}{\cdot}4H_2O$	air	20 CH_4/80H_2 (150 mL/min)	773	1	973	3600	HDO of phenol	[38]
Mo_2C (24) [c]	$(NH_4)6Mo_7O_{24}{\cdot}4H_2O$	air	20 CH_4/80H_2 (150 mL/min)	773	1	973	3600	HDO of phenol	
Mo_2C (21) [d]	$(NH_4)6Mo_7O_{24}{\cdot}4H_2O$	Hydrogen	carbon black	473	10	1113	3600		[18]
Mo_2C (15) [e]	$(NH_4)6Mo_7O_{24}{\cdot}4H_2O$	Hydrogen	carbon black	473	(10 +3)	1113	300		[18]
α-MoC_{1-x} (-)	α-MoO_3		5 n-C_4H_{10}–95H_2			973	14,400	dehydrogenation of benzyl alcohol	[34]
α -Mo_2C (-)	α-MoO_3		20CH4–80H2			1123	14,400	dehydrogenation of benzyl alcohol	[34]
α-Mo_2C (9.1)	$(NH_4)6Mo_7O_{24}{\cdot}4H_2O$		20CH_4–80H_2	473	1	903	18,000	Hydrogenation of CO	[39]
α-Mo_2C (12)	$(NH_4)6Mo_7O_{24}{\cdot}4H_2O$		20CH_4–80H_2	473	1	973	18,000	Hydrogenation of CO	[39]
α-Mo_2C (13.1)	$(NH_4)6Mo_7O_{24}{\cdot}4H_2O$		20CH_4–80H_2	473	7	973	18,000	Hydrogenation of CO	[39]
α-Mo_2C (10.9)	$(NH_4)6Mo_7O_{24}{\cdot}4H_2O$		50CH_4–50H_2	473	1	973	18,000	Hydrogenation of CO	[39]
α-Mo_2C (16.2)	$(NH_4)6Mo_7O_{24}{\cdot}4H_2O$		20CH_4–80H_2	473	1	1073	18,000	Hydrogenation of CO	[39]
α-Mo_2C (10.8)	$(NH_4)6Mo_7O_{24}{\cdot}4H_2O$		10C_2H_6–90H_2	473	1	973	18,000	Hydrogenation of CO	[39]
α-Mo_2C (11.3)	$(NH_4)6Mo_7O_{24}{\cdot}4H_2O$		10C_2H_6–90H_2	473	7	973	36,000	Hydrogenation of CO	[39]
α-Mo_2C (7.3), α-MoC_{1-x}	$(NH_4)6Mo_7O_{24}{\cdot}4H_2O$		5C_4H_{10}–95H_2	473	1	973	18,000	Hydrogenation of CO	[39]
α-Mo_2C (9.5), α-MoC_{1-x}	$(NH_4)6Mo_7O_{24}{\cdot}4H_2O$		5C_4H_{10}–95H_2	473	1	973	36,000	Hydrogenation of CO	[39]
α-Mo_2C (14)	$(NH_4)6Mo_7O_{24}{\cdot}4H_2O$	ethylene glycol	10C_2H_6–90H_2	473	1	1073	18,000	Hydrogenation of CO	[39]
α-Mo_2C (14)	$(NH_4)6Mo_7O_{24}{\cdot}4H_2O$	ethylene glycol	10CH_4–90H_2	573	5	833	14,400		[32]
α-MoC_{1-x}(14)	MoO_3		5C_4H_{10}–95H_2		1	823	3600		[40]
α-Mo_2C (-)	MoO_3		20CH_4–80H_2		1	1023	3600		[40]
α-Mo_2C (-)	MoO_3		10C_2H_6–90H_2		1	9023	3600		[40]
α-Mo_2C (-)	MoO_3		20CH_4–80H_2		1	1023	3600	Partial oxidation of methane	[40]
α-MoC_{1-x}(14)	MoO_3		10C_2H_2–90H_2		1	903	14,400	Partial oxidation of methane	[40]
β -Mo_2C (10–20)	Molybdenum powder		Carbon black			1033	3600		[41]
α-Mo_2C (16.6)	$(NH_4)6Mo_7O_{24}{\cdot}4H_2O$	Hydrogen			1	973	10,800	CO hydrogenation	[42]
η-MoC [f] (-)	$(NH_4)6Mo_7O_{24}{\cdot}4H_2O$	Hydrogen	Glucose	473	5	1073	600	HER	[35]
α-Mo_2C (20) [g]	$(NH_4)6Mo_7O_{24}{\cdot}4H_2O$	Hydrogen	Glucose	473	5	1073	1200	HER	[35]
α-Mo_2C (18)	MoCl5	Hydrogen	Activated carbon		3	873	7200		[24]
α-Mo_2C (16)	MoCl5	Hydrogen	Activated carbon		3	823	1440		[24]
α-Mo_2C (10)	MoCl5	Hydrogen	Activated carbon		3	823	7200		[24]
α-Mo_2C (5)	MoCl5	Hydrogen	Activated carbon		3	723	28,800		[24]
α-Mo_2C (7)	MoCl5	Hydrogen	Activated carbon		3	723	388,800		[24]
α-Mo_2C (8) [h]	MoCl5	Hydrogen	Activated carbon		3	873	7200		[24]
α-Mo_2C (14) [h]	MoCl5	Hydrogen	Activated carbon		3	873	1440		[24]
α-Mo_2C (12)	MoCl5	Hydrogen	Ethanol			1023		HER	[36]
α-Mo_2C (26)	MoCl5	Hydrogen	Ethanol			1123		HER	[36]
α-Mo_2C (27)	MoCl5	Hydrogen	Ethanol			1223		HER	[36]
α-Mo_2C (31)	MoCl5 Hydrogen	MoCl5	Hydrogen	Ethanol		1423		HER	[36]
α-Mo_2C (52)	MoCl5	Hydrogen	Ethanol			1523		HER	[36]
α-Mo_2C (-)	$(NH_4)6Mo_7O_{24}{\cdot}4H_2O$		15CH_4–85H_2	623		863	7200	HDO	[43]
α-Mo_2C (-)	Mo-M-SiO2		methyl in silica		(5 +1)	973	14,400	CO Hydrogenation	[44]
α-Mo_2C (-)	$(NH_4)6Mo_7O_{24}{\cdot}4H_2O$		Aniline		2	1023	18,000	Hydrogen production from methanol	[45]
α-MoC_{1-x}(-)	$(NH_4)6Mo_7O_{24}{\cdot}4H_2O$		Aniline	863	2	948	18,000	Hydrogen production from methanol	[45]

HDO: hydrodeoxygenation; (NH4)6Mo7O24·4H2O: ammonium heptamolybdate; a: Heating rate; b: 6.8 wt% Mo loading; c: 15 wt% Mo loading, d: 50 wt% Mo loading; e: 20 wt% Mo loading; f: 10 min reduction time; g: 20 min reduction time; h: Sample was inserted into pre-heated furnace and kept for the indicated time; HER: Hydrogen Evolution Reaction.
α-MoC_{1-x}: FCC; α-Mo_2C: hexagonal closest-packed (hcp); β-Mo_2C: orthorhombic; γ-MoC: Hexagonal, η-MoC.

supported MCN catalysts and promoted by Co and K where the CNT act as the carbon source. They studied the effect of K/Co and Mo/Co molar ratios on the production of C2+–OH from syngas. Their report shows that the products obtained using unpromoted catalyst during the conversion of CO was predominantly hydrocarbons very at a low conversion. The generation of hydrocarbon was suppressed to some extent upon incorporation of K, thereby favoring formation of alcohol. When Co was introduced at a fixed amount of K, the conversion of CO increases appreciably (from 37.0% to 63.0%). The optimum selectivity to C2+–OH was observed at K/Mo and Mo/Co molar ratios of 0.6 and 1.66, respectively. The enhanced selectivity of higher alcohols may be ascribed to the formation of "Co_3Mo_3C" and "KMo-C" phases, which are suggested to be active for alcohols formation. Table 3 presents the catalytic performance of various promoted/supported MCN catalysts.

From the foregoing, it is tenable to say that careful selection of supporter saves time, exhibits better rate than commercial Cu-Zn-Al catalyst and most of the active oxide supported catalysts. Although the incorporation of the support could incur extra cost of material and process, but the additional cost is worthwhile since supported MCN catalysts are more effective and function at a superior rate, thereby saving time and lowering the cost of using the catalyst for sustainable energy production.

6.3. oxygen-modified molybdenum carbide catalysts

MCN being an oxophilic catalytic materials from both a

Table 2
Catalytic performance of various unsupported MCN catalysts.

Samples	BET surface area (m2/g)/ Pore size (nm)	Reaction	T (K)/ P (MPa)	Performance	Ref.
α-MoC1-x	71.6/2.2[b]	dehydrogenation	393/-	80[b]	[36]
β-Mo_2C	88.9/2.3[b]	dehydrogenation	393/-	100[b]	[36]
MoC550	4.5/-	Hydrogenation of CO	333/3.1	0.071[a]	[43]
MoC630	22.1/-	Hydrogenation of CO	553/3.1	0.074[a]	[43]
MoC700	20.7/-	Hydrogenation of CO	553/3.1	0.078[a]	[43]
MoC760	27.1/-	Hydrogenation of CO	553/3.1	0.081[a]	[43]
Mo_2C	151/-	Hydrogenation of CO	473/4	69[c]	[117]
α-MoC_{1-x}	–	Hydrogenation of CO	473/2	74[c]	[117]
β -Mo_2C	–	Hydrogenation of CO	473/2	29[c]	[118]
Mo_2C	–	Hydrogenation of CO	473/6	32.4[c]	[119]

[a] TOF ($s-1$).
[b] Conversion (%).
[c] Selectivity of ROH.

fundamental point of view and for any potential acid catalysis such as HDO, could be modified with oxygen (O*) to enhance the amount of Brønsted acid sites on its surface without altering the bulk structure of the carbide crystals. The source of O* may be alcohol, H_2O, CO, CO_2 or direct O_2 co-feed at reaction conditions, which dictates the consistent and persistent nature of acid site [125]. O* modified MCN was predicated on deposition of oxygen on the active sites of metallic catalysts during HDO reaction, which poisons the active sites and/or forms Brønsted acid sites [126,127]. Lee et al. [126] observed deposition of carbon and oxygen during an initial transient detected during HDO of anisole over bulk β-Mo_2C to form cyclohexane. The formation of cyclohexane was inhibited by oxygen deposition until finally stopped, leading to formation of benzene. Chen et al. [10] also reported this effect during hydrogenation of benzene and toluene on MCN, which engenders irreversible inhibition of the reaction when methanol or water was co-fed. From the foregoing, it is clear that oxygen deposition under reaction conditions alters the composition and function of MCN catalysts. Therefore, oxygen deposition on MCN prior to utilization for the reaction is promising towards selectivity of a particular product. For instance, [126] compared fresh formulation of MCN with that of O_2-modified MCN catalyst during HDO of anisole to form benzene. Their catalytic activity was almost similar with turnover frequency [128] of $\sim 1.7 \times 10-3\,\mathrm{mol\,mol_{CO}^{-1}\,s^{-1}}$ for the fresh MCN and $\sim 1.5 \times 10–3\,\mathrm{mol\,mol_{CO}^{-1}\,s^{-1}}$; O/Mo bulk (molar ratio) = 0.075. However, the rate of formation of benzene per gram of catalyst was about three times higher on the fresh MCN than the modified MCN, revealing a reduction in the number of sites responsible for benzene formation on MCN. The surface oxidation of MCN takes place in a TPR synthesis technique where O_2 at high pressure is co-feed under certain reaction conditions as dehydration rates increased until a stable value is reached [129].

Sullivan et al. [127] reported a ~ 30-fold increase in the rate of propylene production per gram MCN catalyst from dehydration of isopropyl alcohol at 142 °C when O_2 was co-feed at a pressure range of 0–13.5 kPa. The high rate of isopropyl alcohol dehydration was attributed to the presence of Brønsted acid sites on the catalyst due to modification with oxygen co-feed (0–13.5 kPa). This was confirmed by in situ by 2,6-di-tert-butylpyridine titeration. Sullivan et al. [125] investigated the effect of O* modification on MCN during isopropanol (IPA) dehydration at 142 °C either with 13 kPa O_2 co-feed or under inert He/Ar atmosphere. Their report shows that O_2 co-feed boosted rate of dehydration per gram due to enhancement of the Brønsted acid site resulting from the oxophilicity of MCN.

The source of oxygen plays a vital role on product selectivity on oxygen modified MCN. Chen and Bhan [130] studied the effects of oxygen modification on MCN for HDO of m-cresol over MCN catalysts modified with 1 kPa of H_2O, CO_2, or O_2 at 60 °C. Their report shows that

Table 3
Catalytic performance of various promoted/supported MCN catalysts.

Samples	BET surface area (m2/g)/ Pore size (nm)	Particle size (nm)	Reaction	T (K)/P, MPa	Performance	Ref.
15 MoO_3/TiO_2	65/-	22	HDO	623/2.5	0.0039[a]	[120]
15 Mo_2C/TiO_2	66/-	24	HDO	623/2.5	0.0092[a]	[120]
6.8 Mo_2C/TiO_2	74/-	11	HDO	623/2.5	0.0036[a]	[120]
$PtMo_2C$	-	–	Water Gas Shift	513/-	1.423[g]	[121]
NiMoC-La	142.68/ 7.31	–	methane tri-reforming	1523/-	93.95[b]	[122]
NiMoC-Mg	119.51/ 6.94	–	methane tri-reforming	1523/-	96.05[b]	[122]
NiMoC-K	103.67/ 6.24	–	methane tri-reforming	1523/-	7.32[b]	[122]
NiMoC-Co	129.53/7.42	–	methane tri-reforming	1523/-	99.30[b]	[122]
NiMoC-Ce	132.32/7.26	–	methane tri-reforming	1523/-	98.60[b]	[122]
Co/MoC	–	–	Hydrogenation of CO	603/3.3	4.8[c]	[14]
0.2K/Co-MoC	112/13.12	–	Hydrogenation of CO	603/3.3	42.2[c]	[124]
0.4K/Co-MoC	101/13.39	–	Hydrogenation of CO	603/3.3	44.6[c]	[124]
0.6K/Co-MoC	88/13.53	–	Hydrogenation of CO	603/3.3	48.6[c]	[124]
0.8K/Co-MoC	72/13.76	–	Hydrogenation of CO	603/3.3	41.3[c]	[124]
K/b-Mo_2C/GMC[d]	–	10.8 ± 6.3	Hydrogenation of CO	573/3.0	29.5, 71[f]	[123]
β-Mo_2C/AC[d]	951/ < 2.0	14.3 ± 3.1	Hydrogenation of CO	573/3.0	29.5, 15[f]	[123]
Rh-Mn-Li-Fe/GMC[e]	–	–	Hydrogenation of CO	573/3.0	24.5, 46[f]	[123]
Mo_2C	151	–	Hydrogenation of CO	473/4	69[f]	[113]
Cu/Mo_2C	135	–	Hydrogenation of CO	473/4	76[f]	[117]
α-MoC_{1-x}	–	–	Hydrogenation of CO	473/2	74[f]	[117]
β -Mo_2C	–	–	Hydrogenation of CO	473/2	29[f]	[118]
Cu/Mo_2C	135	–	Hydrogenation of CO	493/6	22[f]	[118]

15 Mo2C/TiO2 = Mo_2C/TiO_2 with ca. 15 wt% of Mo loadings.
[a] TOF (s-1).
[b] WaterGas Shift (mol CO/ mol_{Pt}•s).
[c] H_2 yield at a feed flow rate of 4600 mL h^{-1}.
[d] Selectivity of ROH at varying K/Co molar ratio (from 0.2 to 0.8) and MoCo = 1.66.
[e] 1 wt% Rh, Rh/Mn/Li/Fe = 1/1.9/1.1/0.1.
[f] C2+–OH Selectivity (mol-C%, CO_2-free), Space time yield (mg (h gcat)$^{-1}$).
[g] 5 wt% β-Mo_2C, K/Mo = 0.1.

O_2 exhibits a higher proclivity to deposit oxygen (O/Mo_{bulk} prior to HDO is 0.23 ± 0.02) on fresh MCN, as compared with H_2O and CO_2 (O/Mo_{bulk} prior to HDO is ~ 0.036), as determined by H_2 temperature programmed surface reaction. Excess O/Mo_{bulk} (above ~ 0.06 ± 0.01) poisons the active sites of the catalyst, thereby declining toluene formation as high as 10-fold for O_2 modified MCN compared to the fresh MCN and CO_2 modified MCN. However, the value of TOF is independent of the source of oxygen.

6.4. Effect of temperature and pressure

Temperature and pressure play a vital role in the progress and the product distribution in chemical reaction. Chen et al. [117] investigated the effect of temperature during a low-temperature CO2 hydrogenation Mo_2C supported metal catalysts. The reaction progressed feeding 10 bar CO2 and 30 bar H_2 through a dip tube after removing the dissolved oxygen by purging the solvents with H_2 for 15 min at temperatures of 135–200 °C. The report showed a significant increase in conversion and improved product distribution when the temperature was increased from 135 to 200 °C (Table 4). The remarkable improvement in performance is due to increase in the solubility of H_2 from 0.14 to 0.18 mol/L as the temperature increased from 135 to 200 °C [131,132].

Boullosa-Eiras et al. [120] studied the effect of pressure on the equilibrium composition. Their report shows a low consumption of H2 at a pressure less than 30 bar, which favors a rather larger amount of benzene. N-hexane rather than benzene was favored at higher pressure. The report of Chen and Bhan [130] on the effect of pressure on m-cresol HDO shows that the TOF of toluene increases as the H_2 pressure was raised from 10 to 110 kPa. However, the performance was independent of m-cresol pressure.

7. Conclusion

Definitely, hydrogenation and hydrogen production reactions are the modern research hotspot towards renewable and sustainable energy production and have, therefore, inspired extensive interests in rational design and synthesis of cheap, noble metal-free, thermal/hydrothermal stable and active catalysts. This will offer a remarkable relief to the renewable and sustainable energy community. One of such materials is MCN, which is a promising replacement for noble metals. Factors like carbon source, pre-treatment temperature TpreT, heating rate, Mo loading, carburization temperature (Tcarb), carburization time (tcarb), Mo-precursor and crystalline phases significantly influence the design of MNC by varying the crystalline Mo-phases of MNC.

High pretreatment temperature favors formation of MNC rather than low temperature as there is the formation of a large amount of crystalline MoO_2 phase at a low pretreatment temperature rather than MCN due to incomplete carburization of the precursor. The reverse is the case with a high pretreatment temperature, which leads to the formation of a large amount of MCN resulting from a high reduction rate of MoO_2.

Lowering the heating rate favors early carburation leading to lower carburation temperature and formation of a larger particle size when compared with a higher heating rate. At a higher heating rate, the carburation temperature becomes high leading to sintering of the carbide phase of the sample. The increase in carburation temperature leads to increase in the carburation of the precursor, which favors formation of MCN. Low carburation temperature exhibits predominantly crystalline MoO_2 phase. Therefore, for rational design of MCN, it is required to employ a long chain hydrocarbon as the carbon source and a combination of high pretreatment temperature, lowered heating rate, high carburation temperature and high carburation time.

The operating condition, as well as preparation method, is also responsible for the structural diversity. Therefore, the understanding of this diversity is also vital to the suitability of MCN for industrial application. MCN is classified into α-MoC1–x, α-Mo2C, β-Mo2C, γ-MoC, and η-MoC. α-Mo_2C, γ-MoC and η-MoC exhibit hcp structure, α-MoC1–x is fcc, while β-Mo_2C is orthorhombic. Out of the MCN, are α-MoC1–x and β-Mo_2C are more stable and exhibit a remarkable electrochemical performance due to their large ionic contribution. β-Mo_2C is a viable substitute for the commercial Cu-based catalysts used in Water-Gas-Shift (WGS) reaction while α-Mo_2C is highly suitable for dehydrogenation process. The functionality of these structures largely depends on the surface properties.

The reaction mechanism of MCN is better explained by multiscale reaction model (QM/MM), which combines quantum mechanical (QM) density functional tight-binding (DFTB) technique with a molecular mechanical (MM) force field. However, the computational cost has been the challenge. To reduce the computation cost of multiscale model while maintaining high numerical accuracy and reusability of the functional form for other systems, neural-network (NN) is considered suitable for representation of the ab initio potential energy surface (PES). NN PES has the capacity to produce a similar result with that DFT at a small fraction of the computational costs. A more promising approach is the use of extreme learning machine (ELM), which was developed from NN. ELM is extremely faster in learning, suitable for high-dimensional potentials, and better in term of generalization capability, making it more cost-sensitive and efficient.

The catalytic activity of MCN based catalyst (both unsupported and supported/promoted) was investigated, showing the need for support/

Table 4
CO_2 hydrogenation rates and selectivities over Mo_2C and M/Mo_2C catalysts.[a]

Catalysts	Trxn (K)	CO2 conv.rate/TOF[b]		Selectivity (%)[c,d]							Ref.
		μmol/m_2/s·10^4	$s^{-1}\cdot10^4$	MeOH	EtOH	CO	CH4	C2H4	C2H6	C3+	
Mo_2C	408	1.7	0.6	79	0	16	5.3	0	0	0	[133]
	473	55	20	53	16	4.9	17	0.8	5.0	3.0	[133]
Cu/Mo_2C	408	4.6	2.1	93	0	4.1	2.6	0	0	0	[117]
	473	90	41	63	14	8.6	9.8	0.3	3.7	1.9	[117]
Pd/Mo_2C	408	5.9	2.3	95	0	3.6	1.6	0	0	0	[117]
	473	97	39	68	11	9.6	7.6	0.3	2.5	1.3	[117]
Co/Mo_2C	408	4.8	1.9	84	0	5.7	9.4	0	1.1	0.1	[117]
	473	86	35	46	25	9.5	9.5	0.6	5.6	1.4	[117]
Fe/Mo_2C	408	3.9	1.5	87	0	4.1	7.2	0	1.2	0.6	[117]
	473	99	38	58	16	6.8	8.1	0.4	6.3	3.8	[117]

[a] 10 bar CO2, 30 bar H_2, 37.5 mL 1,4-dioxane and 200 mg catalyst.
[b] Calculated at 2 h.
[c] Calculated at ~ 1.0% CO_2 conversion at 135 °C and ~ 10% CO_2 conversion at 200 °C. The selectivities were calculated on a C_1 basis.
[d] C_3 contains C_3H_6 and C_3H_8, and C_4 contains C_4H_8 and C_4H_{10}.

promoter. Addition of support/promoter enhanced the catalytic performance of MCN based catalyst with respect to conversion, TOF as well as product distribution.

Acknowledgments

The authors gratefully acknowledge the financial support from GSP-MOHE (MO008–2015) High Impact Research (HIR) grant and RP015–2012D grant, University of Malaya, Malaysia.

References

[1] Alaba PA, Sani YM, Daud WMaW. Kaolinite properties and advances for solid acid and basic catalyst synthesis. RSC Adv 2015;5:101127–47.
[2] Alaba PA, Sani YM, Daud WMaW. Efficient biodiesel production via solid superacid catalysis: a critical review on recent breakthrough. RSC Adv 2016.
[3] Alaba PA, Sani YM, Mohammed IY, Daud W, Ashri WM. Insight into catalyst deactivation mechanism and suppression techniques in thermocatalytic deoxygenation of bio-oil over zeolites. Rev Chem Eng 2016;32:71–91.
[4] Mcnab WW, Ruiz R, Reinhard M. In-situ destruction of chlorinated hydrocarbons in groundwater using catalytic reductive dehalogenation in a reactive well: testing and operational experiences. Environ Sci Technol 2000;34:149–53.
[5] Tominaga H, Aoki Y, Nagai M. Hydrogenation of CO on molybdenum and cobalt molybdenum carbides. Appl Catal A: General 2012;423:192–204.
[6] Jongerius AL, Gosselink RW, Dijkstra J, Bitter JH, Bruijnincx PC, Weckhuysen BM. Carbon nanofiber supported transition-metal carbide catalysts for the Hydrodeoxygenation of Guaiacol. ChemCatChem 2013;5:2964–72.
[7] Wang P, Qi J, Chen X, Li C, Wang T, Liang C. New insights into high-valence state Mo in molybdenum carbide nanobelts for hydrogen evolution reaction. Int J Hydrog Energy 2017;42:10880–90.
[8] Tang C, Wu Z, Wang D. Influence of carbon on molybdenum carbide catalysts for the hydrogen evolution reaction. ChemCatChem 2016;8:1961–7.
[9] Zaman S, Smith KJ. A review of molybdenum catalysts for synthesis gas conversion to alcohols: catalysts, mechanisms and kinetics. Catal Rev 2012;54:41–132.
[10] Chen C-J, Lee W-S, Bhan A. Mo 2 C catalyzed vapor phase hydrodeoxygenation of lignin-derived phenolic compound mixtures to aromatics under ambient pressure. Appl Catal A: General 2016;510:42–8.
[11] Wang S, Wang J, Zhu M, Bao X, Xiao B, Su D, Li H, Wang Y. Molybdenum-carbide-modified nitrogen-doped carbon vesicle encapsulating nickel nanoparticles: a highly efficient, low-cost catalyst for hydrogen evolution reaction. J Am Chem Soc 2015;137:15753–9.
[12] Regmi YN, Wan C, Duffee KD, Leonard BM. Nanocrystalline Mo2C as a bifunctional water splitting electrocatalyst. ChemCatChem 2015;7:3911–5.
[13] Tang C, Wang W, Sun A, Qi C, Zhang D, Wu Z, Wang D. Sulfur-decorated molybdenum carbide catalysts for enhanced hydrogen evolution. ACS Catalysis 2015;5:6956–63.
[14] Namiki T, Yamashita S, Tominaga H, Nagai M. Dissociation of CO and H 2 O during water–gas shift reaction on carburized Mo/Al 2 O 3 catalyst. Appl Catal A: General 2011;398:155–60.
[15] Sundaramurthy V, Dalai A, Adjaye J. HDN and HDS of different gas oils derived from Athabasca bitumen over phosphorus-doped NiMo/γ-Al2O3 carbides. Appl Catal B: Environ 2006;68:38–48.
[16] Oshikawa K, Nagai M, Omi S. Characterization of molybdenum carbides for methane reforming by TPR, XRD, and XPS. J Phys Chem B 2001;105:9124–31.
[17] Al-Megren HA, González-Cortés SL, Xiao T, Green ML. A comparative study of the catalytic performance of Co-Mo and Co (Ni)-W carbide catalysts in the hydrodenitrogenation (HDN) reaction of pyridine. Appl Catal A: Gen 2007;329:36–45.
[18] Nguyen TH, Nguyen TV, Lee YJ, Safinski T, Adesina AA. Structural evolution of alumina supported Mo–W carbide nanoparticles synthesized by precipitation from homogeneous solution. Mater Res Bull 2005;40:149–57.
[19] Guil-López R, Nieto E, Botas J, Fierro J. On the genesis of molybdenum carbide phases during reduction-carburization reactions. J Solid State Chem 2012;190:285–95.
[20] Ojha K, Saha S, Kolev H, Kumar B, Ganguli AK. Composites of graphene-Mo 2 C rods: highly active and stable electrocatalyst for hydrogen evolution reaction. Electrochim Acta 2016;193:268–74.
[21] Guil-López R, Martínez-Huerta M, Guillén-Villafuerte O, Peña M, Fierro J, Pastor E. Highly dispersed molybdenum carbide as non-noble electrocatalyst for PEM fuel cells: performance for CO electrooxidation. Int J Hydrog Energy 2010;35:7881–8.
[22] Weigert EC, Esposito DV, Chen JG. Cyclic voltammetry and X-ray photoelectron spectroscopy studies of electrochemical stability of clean and Pt-modified tungsten and molybdenum carbide (WC and Mo 2 C) electrocatalysts. J Power Sources 2009;193:501–6.
[23] Nagai M, Yoshida M, Tominaga H. Tungsten and nickel tungsten carbides as anode electrocatalysts. Electrochim Acta 2007;52:5430–6.
[24] Wang T, Wang S, Li Y-W, Wang J, Jiao H. Adsorption equilibria of CO coverage on β-Mo2C surfaces. J Phys Chem C 2012;116:6340–8.
[25] Pielaszek J, Mierzwa B, Medjahdi G, Marêché J, Puricelli S, Celzard A, Furdin G. Molybdenum carbide catalyst formation from precursors deposited on active carbons: XRD studies. Appl Catal A: General 2005;296:232–7.
[26] Lee JS, Oyama S, Boudart M. Molybdenum carbide catalysts: I. Synthesis of unsupported powders. J Catal 1987;106:125–33.
[27] Alaba PA, Abbas A, Daud WMW. Insight into catalytic reduction of CO 2: Catalysis and reactor design. J Clean Prod 2016.
[28] Mordenti D, Brodzki D, Djéga-Mariadassou G. New synthesis of Mo 2 C 14 nm in average size supported on a high specific surface area carbon material. J Solid State Chem 1998;141:114–20.
[29] Furimsky E. Metal carbides and nitrides as potential catalysts for hydroprocessing. Appl Catal A: Gen 2003;240:1–28.
[30] Lewandowski M, Szymańska-Kolasa A, Da Costa P, Sayag C. Catalytic performances of platinum doped molybdenum carbide for simultaneous hydrodenitrogenation and hydrodesulfurization. Catal Today 2007;119:31–4.
[31] Hsu IJ, Hansgen DA, Mccandless BE, Willis BG, Chen JG. Atomic layer deposition of Pt on tungsten monocarbide (WC) for the oxygen reduction reaction. J Phys Chem C 2011;115:3709–15.
[32] Esposito DV, Hunt ST, Stottlemyer AL, Dobson KD, Mccandless BE, Birkmire RW, Chen JG. Low-cost hydrogen-evolution catalysts based on monolayer platinum on tungsten monocarbide substrates. Angew Chem Int Ed 2010;49:9859–62.
[33] Tate Iii RL, Alexander M. Stability of nitrosamines in samples of lake water, soil, and sewage 2. J Natl Cancer Inst 1975;54:327–30.
[34] Guzmán HJ, Xu W, Stacchiola D, Vitale G, Scott CE, Rodríguez JA, Pereira-Almao P. Formation of β-Mo 2C below 600 °C using MoO 2 nanoparticles as precursor. J Catal 2015;332:83–94.
[35] Ranhotra G, Haddix G, Bell A, Reimer J. Catalysis over molybdenum carbides and nitrides: I. Catalyst characterization. J Catal 1987;108:24–39.
[36] Li Z, Chen C, Zhan E, Ta N, Li Y, Shen W. Crystal-phase control of molybdenum carbide nanobelts for dehydrogenation of benzyl alcohol. Chem Commun 2014;50:4469–71.
[37] Tang C, Sun A, Xu Y, Wu Z, Wang D. High specific surface area Mo 2C nanoparticles as an efficient electrocatalyst for hydrogen evolution. J Power Sources 2015;296:18–22.
[38] Alhajri NS, Anjum DH, Takanabe K. Molybdenum carbide–carbon nanocomposites synthesized from a reactive template for electrochemical hydrogen evolution. J Mater Chem A 2014;2:10548–56.
[39] Hare J, Hsu W, Kroto H, Lappas A, Prassides K, Terrones M, Walton D. Nanoscale encapsulation of molybdenum carbide in carbon clusters. Chem Mater 1996;8:6–8.
[40] Saito Y, Matsumoto T, Nishikubo K. Encapsulation of carbides of chromium, molybdenum and tungsten in carbon nanocapsules by arc discharge. J Cryst Growth 1997;172:163–70.
[41] Xiao T, York AP, Coleman KS, Claridge JB, Sloan J, Charnock J, Green ML. Effect of carburising agent on the structure of molybdenum carbides. J Mater Chem 2001;11:3094–8.
[42] Torabi O, Golabgir MH, Tajizadegan H, Torabi H. A study on mechanochemical behavior of MoO 3–Mg–C to synthesize molybdenum carbide. Int J Refract Met Hard Mater 2014;47:18–24.
[43] Mo T, Xu J, Yang Y, Li Y. Effect of carburization protocols on molybdenum carbide synthesis and study on its performance in CO hydrogenation. Catal Today 2016;261:101–15.
[44] Ma Y, Guan G, Phanthong P, Li X, Cao J, Hao X, Wang Z, Abudula A. Steam reforming of methanol for hydrogen production over nanostructured wire-like molybdenum carbide catalyst. Int J Hydrog Energy 2014;39:18803–11.
[45] Posada-Pérez S, Viñes F, Ramirez PJ, Vidal AB, Rodriguez JA, Illas F. The bending machine: CO 2 activation and hydrogenation on δ-MoC (001) and β-Mo 2C (001) surfaces. Phys Chem Chem Phys 2014;16:14912–21.
[46] Wang T, Tian X, Yang Y, Li Y-W, Wang J, Beller M, Jiao H. Coverage dependent adsorption and co-adsorption of CO and H 2 on the CdI 2-antitype metallic Mo 2C (001) surface. Phys Chem Chem Phys 2015;17:1907–17.
[47] Rodriguez JA, Evans J, Feria L, Vidal AB, Liu P, Nakamura K, Illas F. CO 2 hydrogenation on Au/TiC, Cu/TiC, and Ni/TiC catalysts: production of CO, methanol, and methane. J Catal 2013;307:162–9.
[48] Kosanović C, Havancsák K, Subotić B, Svetličić V, Radić TM, Cziráki Á, Huhn G, Buljan I, Smrečki V. Study of the mechanism of formation of nano-crystalline zeolite X in heterogeneous system. Microporous Mesoporous Mater 2011;142:139–46.
[49] Wu W, Wu Z, Liang C, Chen X, Ying P, Li C. In situ FT-IR spectroscopic studies of CO adsorption on fresh Mo2C/Al2O3 catalyst. J Phys Chem B 2003;107:7088–94.
[50] Miyao T, Shishikura I, Matsuoka M, Nagai M, Oyama S. Preparation and characterization of alumina-supported molybdenum carbide. Appl Catal A: Gen 1997;165:419–28.
[51] Hwu HH, Chen JG. Surface chemistry of transition metal carbides. Chem Rev 2005;105:185–212.
[52] Bokhonov B, Borisova Y, Korchagin M. Formation of encapsulated molybdenum carbide particles by annealing mechanically activated mixtures of amorphous carbon with molybdenum. Carbon 2004;42:2067–71.
[53] Gao J, Zheng Y, Fitzgerald GB, De Joannis J, Tang Y, Wachs IE, Podkolzin SG. Structure of Mo2C x and Mo4C x molybdenum carbide nanoparticles and their anchoring sites on ZSM-5 zeolites. J Phys Chem C 2014;118:4670–9.
[54] Zhong Y, Xia X, Shi F, Zhan J, Tu J, Fan HJ. Transition metal carbides and nitrides in energy storage and conversion. Adv Sci 2016.
[55] Politi JR Dos Santos, Viñes F, Rodriguez JA, Illas F. Atomic and electronic structure of molybdenum carbide phases: bulk and low Miller-index surfaces. Phys Chem Chem Phys 2013;15:12617–25.
[56] Pistonesi C, Pronsato ME, Bugyi LS, Juan A. Theoretical model for CO adsorption and dissociation on clean and K-doped β-Mo2C surfaces. J Phys Chem C 2012;116:24573–81.
[57] Rocha AS, Rocha AB, Silva VT Da. Benzene adsorption on Mo 2C: a theoretical and experimental study. Appl Catal A: Gen 2010;379:54–60.
[58] Hugosson HW, Jansson U, Johansson B, Eriksson O. Phase stability diagrams of

transition metal carbides, a theoretical study. Chem Phys Lett 2001;333:444–50.
[59] Ma R, Hao W, Ma X, Tian Y, Li Y. Catalytic ethanolysis of kraft lignin into high-value small-molecular chemicals over a nanostructured α-molybdenum carbide catalyst. Angew Chem Int Ed 2014;53:7310–5.
[60] Wang T, Liu X, Wang S, Huo C, Li Y-W, Wang J, Jiao H. Stability of β-Mo2C facets from ab initio atomistic thermodynamics. J Phys Chem C 2011;115:22360–8.
[61] Liu P, Rodriguez JA. Effects of carbon on the stability and chemical performance of transition metal carbides: a density functional study. J Chem Phys 2004;120:5414–23.
[62] Liu P, Rodriguez JA. Catalytic properties of molybdenum carbide, nitride and phosphide: a theoretical study. Catal Lett 2003;91:247–52.
[63] Hugosson HW, Nordström L, Jansson U, Johansson B, Eriksson O. Theoretical studies of substitutional impurities in molybdenum carbide. Phys Rev B 1999;60:15123.
[64] Otani S, Ishizawa Y. Preparation of Mo 2C single crystals by the floating zone method. J Cryst Growth 1995;154:202–4.
[65] Fries R, Kempter CP. 195. Dimolybdenum carbide. Anal Chem 1960;32. [1898-1898].
[66] Jhi S-H, Ihm J, Louie SG, Cohen ML. Electronic mechanism of hardness enhancement in transition-metal carbonitrides. Nature 1999;399:132–4.
[67] Hanif A, Xiao T, York AP, Sloan J, Green ML. Study on the structure and formation mechanism of molybdenum carbides. Chem Mater 2002;14:1009–15.
[68] Liao L, Wang S, Xiao J, Bian X, Zhang Y, Scanlon MD, Hu X, Tang Y, Liu B, Girault HH. A nanoporous molybdenum carbide nanowire as an electrocatalyst for hydrogen evolution reaction. Energy Environ Sci 2014;7:387–92.
[69] Gao Q, Zhang C, Xie S, Hua W, Zhang Y, Ren N, Xu H, Tang Y. Synthesis of nanoporous molybdenum carbide nanowires based on organic- inorganic hybrid nanocomposites with sub-nanometer periodic structures. Chem Mater 2009;21:5560–2.
[70] Chen W-F, Wang C-H, Sasaki K, Marinkovic N, Xu W, Muckerman J, Zhu Y, Adzic R. Highly active and durable nanostructured molybdenum carbide electrocatalysts for hydrogen production. Energy Environ Sci 2013;6:943–51.
[71] Viñes F, Rodriguez JA, Liu P, Illas F. Catalyst size matters: tuning the molecular mechanism of the water–gas shift reaction on titanium carbide based compounds. J Catal 2008;260:103–12.
[72] Liu P, Rodriguez JA. Water-gas-shift reaction on molybdenum carbide surfaces: essential role of the oxycarbide. J Phys Chem B 2006;110:19418–25.
[73] Zheng W, Cotter TP, Kaghazchi P, Jacob T, Frank B, Schlichte K, Zhang W, Su DS, SchüTh F, SchlöGl R. Experimental and theoretical investigation of molybdenum carbide and nitride as catalysts for ammonia decomposition. J Am Chem Soc 2013;135:3458–64.
[74] Medford AJ, Vojvodic A, Studt F, Abild-Pedersen F, Nørskov JK. Elementary steps of syngas reactions on Mo 2C (001): adsorption thermochemistry and bond dissociation. J Catal 2012;290:108–17.
[75] Yang Y, Evans J, Rodriguez JA, White MG, Liu P. Fundamental studies of methanol synthesis from CO 2 hydrogenation on Cu (111), Cu clusters, and Cu/ZnO (0001 [combining macron]). Phys Chem Chem Phys 2010;12:9909–17.
[76] Vidal AB, Feria L, Evans J, Takahashi Y, Liu P, Nakamura K, Illas F, Rodriguez JA. CO_2 activation and methanol synthesis on novel Au/TiC and Cu/TiC catalysts. J Phys Chem Lett 2012;3:2275–80.
[77] Lo R-L, Fukui K-I, Otani S, Iwasawa Y. High resolution images of Mo 2C (0001)-(3× 3) R30° structure by scanning tunneling microscopy. Surf Sci 1999;440:L857–62.
[78] Clair TPS, Oyama ST, Cox DF, Otani S, Ishizawa Y, Lo R-L, Fukui K-I, Iwasawa Y. Surface characterization of α-Mo 2C (0001). Surf Sci 1999;426:187–98.
[79] Sugihara M, Ozawa K-I, Edamoto K, Otani S. Photoelectron spectroscopy study of Mo 2C (0001). Solid State Commun 2001;121:1–5.
[80] Kato M, Sato T, Ozawa K, Edamoto K, Otani S. Surface electronic structure of α-Mo 2C (0001). Surf Sci 2006;600:448–52.
[81] Wang T. About CO and H2 activation mechanisms on Fe and Mo2C catalysts on the basis of density functional theory computation and ab initio atomistic thermodynamics. Leibniz-Institut für Katalyse e.V. an der, 29a. Rostock, Germany: Universität Rostock, Albert-Einstein Strasse; 2014. p. 131.
[82] Liu X, Salahub DR. Molybdenum carbide nanocatalysts at work in the in situ environment: a density functional tight-binding and quantum mechanical/molecular mechanical study. J Am Chem Soc 2015;137:4249–59.
[83] Shen L, Wu J, Yang W. Multiscale quantum mechanics/molecular mechanics simulations with neural networks. J Chem Theory Comput 2016.
[84] Tahamtan I, Afshar AS, Ahamdzadeh K. Factors affecting number of citations: a comprehensive review of the literature. Scientometrics 2016;107:1195–225.
[85] Brenner DW, Garrison BJ. Dissociative valence force field potential for silicon. Phys Rev B 1986;34:1304.
[86] Tersoff J. New empirical approach for the structure and energy of covalent systems. Phys Rev B 1988;37:6991.
[87] Baskes M. Modified embedded-atom potentials for cubic materials and impurities. Phys Rev B 1992;46:2727.
[88] Cornell WD, Cieplak P, Bayly CI, Gould IR, Merz KM, Ferguson DM, Spellmeyer DC, Fox T, Caldwell JW, Kollman PA. A second generation force field for the simulation of proteins, nucleic acids, and organic molecules. J Am Chem Soc 1995;117:5179–97.
[89] Behler J. Neural network potential-energy surfaces in chemistry: a tool for large-scale simulations. Phys Chem Chem Phys 2011;13:17930–55.
[90] Press WH. Numerical recipes 3rd edition: the art of scientific computing. Cambridge University Press; 2007.
[91] Bartók AP, Payne MC, Kondor R, Csányi G. Gaussian approximation potentials: the accuracy of quantum mechanics, without the electrons. Phys Rev Lett 2010;104:136403.
[92] Jordan MJ, Thompson KC, Collins MA. Convergence of molecular potential energy surfaces by interpolation: application to the OH + H2→ H2O + H reaction. J Chem Phys 1995;102:5647–57.
[93] Makarov DE, Metiu H. Fitting potential-energy surfaces: a search in the function space by directed genetic programming. J Chem Phys 1998;108:590–8.
[94] Zhou SK, Chellappa R. From sample similarity to ensemble similarity: probabilistic distance measures in reproducing kernel hilbert space. IEEE Trans Pattern Anal Mach Intell 2006;28:917.
[95] Jiang B, Guo H. Permutation invariant polynomial neural network approach to fitting potential energy surfaces. J Chem Phys 2013;139:054112.
[96] Guo Y, Kawano A, Thompson DL, Wagner AF, Minkoff M. Interpolating moving least-squares methods for fitting potential energy surfaces: applications to classical dynamics calculations. J Chem Phys 2004;121:5091–7.
[97] Eshet H, Khaliullin RZ, Kühne TD, Behler J, Parrinello M. Ab initio quality neural-network potential for sodium. Phys Rev B 2010;81:184107.
[98] Silva ME, Acioli PH, Pedroza AC. Estimating correlation energy of diatomic molecules and atoms with neural networks. J Comput Chem 1997;18:1407–14.
[99] Wu J, Xu X. Improving the B3LYP bond energies by using the X1 method. J Chem Phys 2008;129:164103.
[100] Urata S, Takada A, Uchimaru T, Chandra AK, Sekiya A. Artificial neural network study for the estimation of the C–H bond dissociation enthalpies. J Fluor Chem 2002;116:163–71.
[101] Yao X, Zhang X, Zhang R, Liu M, Hu Z, Fan B. Prediction of enthalpy of alkanes by the use of radial basis function neural networks. Comput Chem 2001;25:475–82.
[102] Duan X-M, Li Z-H, Song G-L, Wang W-N, Chen G-H, Fan K-N. Neural network correction for heats of formation with a larger experimental training set and new descriptors. Chem Phys Lett 2005;410:125–30.
[103] Balabin RM, Lomakina EI. Neural network approach to quantum-chemistry data: accurate prediction of density functional theory energies. J Chem Phys 2009;131:074104.
[104] Artrith N, Behler J. High-dimensional neural network potentials for metal surfaces: a prototype study for copper. Phys Rev B 2012;85:045439.
[105] Manzhos S, Carrington Jr T. Using redundant coordinates to represent potential energy surfaces with lower-dimensional functions. J Chem Phys 2007;127:014103.
[106] Malshe M, Narulkar R, Raff L, Hagan M, Bukkapatnam S, Agrawal P, Komanduri R. Development of generalized potential-energy surfaces using many-body expansions, neural networks, and moiety energy approximations. J Chem Phys 2009;130:184102.
[107] Behler J. Constructing high-dimensional neural network potentials: a tutorial review. Int J Quantum Chem 2015;115:1032–50.
[108] Behler J. Representing potential energy surfaces by high-dimensional neural network potentials. J Phys: Condens Matter 2014;26:183001.
[109] Sosso GC, Miceli G, Caravati S, Behler J, Bernasconi M. Neural network interatomic potential for the phase change material GeTe. Phys Rev B 2012;85:174103.
[110] Behler J, Parrinello M. Generalized neural-network representation of high-dimensional potential-energy surfaces. Phys Rev Lett 2007;98:146401.
[111] Nguyen-Truong HT, Le HM. An implementation of the Levenberg–Marquardt algorithm for simultaneous-energy-gradient fitting using two-layer feed-forward neural networks. Chem Phys Lett 2015;629:40–5.
[112] Huang G-B, Zhu Q-Y, Siew C-K. Extreme learning machine: theory and applications. Neurocomputing 2006;70:489–501.
[113] Lu S, Wang X, Zhang G, Zhou X. Effective algorithms of the Moore-Penrose inverse matrices for extreme learning machine. Intell Data Anal 2015;19:743–60.
[114] Wang X, Chen A, Feng H. Upper integral network with extreme learning mechanism. Neurocomputing 2011;74:2520–5.
[115] Yin J-C. A variable-structure online sequential extreme learning machine for time-varying system prediction. Neurocomputing 2017;261:115–25.
[116] Posada-Pérez S, Viñes F, Valero R, Rodriguez JA, Illas F. Adsorption and dissociation of molecular hydrogen on orthorhombic β-Mo 2C and cubic δ-MoC (001) surfaces. Surf Sci 2017;656:24–32.
[117] Chen Y, Choi S, Thompson LT. Low temperature CO 2 hydrogenation to alcohols and hydrocarbons over Mo 2C supported metal catalysts. J Catal 2016;343:147–56.
[118] Xu W, Ramirez PJ, Stacchiola D, Rodriguez JA. Synthesis of α-MoC1-x and β-MoCy catalysts for CO_2 hydrogenation by thermal carburization of Mo-oxide in hydrocarbon and hydrogen mixtures. Catal Lett 2014;144:1418–24.
[119] Dubois J-L, Sayama K, Arakawa H. CO_2 hydrogenation over carbide catalysts. Chem Lett 1992;21:5–8.
[120] Boullosa-Eiras S, Lødeng R, Bergem H, Stöcker M, Hannevold L, Blekkan EA. Catalytic hydrodeoxygenation (HDO) of phenol over supported molybdenum carbide, nitride, phosphide and oxide catalysts. Catal Today 2014;223:44–53.
[121] Schweitzer NM, Schaidle JA, Ezekoye OK, Pan X, Linic S, Thompson LT. High activity carbide supported catalysts for water gas shift. J Am Chem Soc 2011;133:2378–81.
[122] Zou H, Chen S, Huang J, Zhao Z. Effect of additives on the properties of nickel molybdenum carbides for the tri-reforming of methane. Int J Hydrog Energy 2016;41:16842–50.
[123] Chai S-H, Schwartz V, Howe JY, Wang X, Kidder M, Overbury SH, Dai S, Jiang D-E. Graphitic mesoporous carbon-supported molybdenum carbides for catalytic hydrogenation of carbon monoxide to mixed alcohols. Microporous Mesoporous Mater 2013;170:141–9.
[124] Kiai RM, Nematian T, Tavasoli A, Karimi A. Effect of elemental molar ratio on the synthesis of higher alcohols over Co-promoted alkali-modified Mo 2C catalysts supported on CNTs. J Energy Chem 2015;24:278–84.

[125] Sullivan MM, Bhan A. Acid site densities and reactivity of oxygen-modified transition metal carbide catalysts. J Catal 2016;344:53–8.
[126] Lee W-S, Kumar A, Wang Z, Bhan A. Chemical titration and transient kinetic studies of site requirements in Mo2C-catalyzed vapor phase anisole hydrodeoxygenation. ACS Catal 2015;5:4104–14.
[127] Sullivan MM, Held JT, Bhan A. Structure and site evolution of molybdenum carbide catalysts upon exposure to oxygen. J Catal 2015;326:82–91.
[128] Moser P, Schmidt S, Sieder G, Garcia H, Stoffregen T. Performance of MEA in a long-term test at the post-combustion capture pilot plant in Niederaussem. Int J Greenh Gas Control 2011;5:620–7.
[129] Delannoy L, Giraudon J-M, Granger P, Leclercq L, Leclercq G. Group VI transition metal carbides as alternatives in the hydrodechlorination of chlorofluorocarbons. Catal Today 2000;59:231–40.
[130] Chen C-J, Bhan A. Mo2C modification by CO2, H2O, and O2: effects of oxygen content and oxygen source on rates and selectivity of m-cresol hydrodeoxygenation. ACS Catal 7. 2017. p. 1113–22.
[131] Brunner E. Solubility of hydrogen in 10 organic solvents at 298.15, 323.15, and 373.15 K. J Chem Eng Data 1985;30:269–73.
[132] Kassim D, Zainel H, Al-Asaf S, Talib E. The temperature dependence of the solubility of carbon dioxide in several extraction solvents. Fluid Phase Equilib 1988;41:287–94.
[133] Chen Y, Choi S, Thompson LT. Low-temperature CO_2 hydrogenation to liquid products via a heterogeneous cascade catalytic system. ACS Catalysis 5. 2015. p. 1717–25.